

An Analysis on the Parton Distribution Functions of Heavy Mesons

Satyajit Puhan ^{1,2,*}

¹*Computational High Energy Physics Lab, Department of Physics,
Dr. B.R. Ambedkar National Institute of Technology, Jalandhar, Punjab 144008, India*
²*Institute of Physics, Academia Sinica, Taipei 11529, Taiwan*

In this work, we investigate the constituent parton distribution functions (PDFs) of the kaon and heavy pseudoscalar mesons within the light-cone quark model. Starting from the initial scale quark and antiquark PDFs, obtained by evaluating the quark–quark correlation functions for individual mesons, we perform quantum chromodynamics (QCD) evolution to determine the partonic structure at higher energy scales. The QCD evolution has been carried out through the next-to-leading order (NLO) Dokshitzer–Gribov–Lipatov–Altarelli–Parisi (DGLAP) equations. We further compute the average longitudinal momentum fractions carried by the individual constituents both at the model scale and evolved scale. In addition, the NLO structure functions for the kaon are predicted at higher energy scales relevant for the upcoming Electron–Ion Collider (EIC). For the COMPASS++/AMBER experiment, we further present detailed predictions for the NLO Drell–Yan cross sections corresponding to both isospin states of the kaon, employing Carbon, Tungsten, and Aluminum as nuclear targets. We demonstrate the dominance of the heavy constituents over the lighter constituents within their heavy mesons in terms of their possessed momentum fractions.

I. INTRODUCTION

It has been a challenging task to describe the internal structure of hadrons in terms of the constituent quarks, antiquarks, gluons and sea-quarks. These constituents are primarily responsible for all the phenomena happening within the hadron and its interaction with other hadrons. The strong interactions among the partons within the hadron and the hadronic matrix elements of quark-gluon field operators can be understood by using quantum chromodynamics (QCD) [1]. QCD factorization theorems are used to separate the long-distance non-perturbative components from the short-distance perturbative contributions in experimental cross-sections, allowing for the study of hadron structure. The theoretical description of the hadronic structure in the perturbative zone becomes extremely non-trivial due to the complex dynamics of sea quarks, gluons, and valence quarks inside the hadrons. So, the distribution of these quarks and gluons can be studied using the quark-gluon correlation functions in the non-perturbative region through low-energy scale models [2–6]. Because of the non-perturbative nature of QCD, especially color confinement and spontaneous chiral symmetry breaking, it remains difficult to understand hadron structure directly from first principles and to perform calculations starting from the fundamental QCD Lagrangian [7, 8]. The distribution functions of the constituents encode information about various multi-dimensional degrees of freedom, including their momentum and spatial distributions. These distribution functions are generalized transverse momentum parton distribution functions (GTMDs) [9–11], generalized parton distributions (GPDs) [12–17], transverse momentum parton distribution functions (TMDs) [18–

23], parton distribution functions (PDFs) [24–26], form factors (FFs) [27, 28], etc.

The one-dimensional PDFs is one of the most fundamental non-perturbative inputs in QCD, encoding the longitudinal momentum structure of quarks and gluons inside the hadrons. Determining the PDFs of different hadrons by studying hard-scattering phenomena is one of the main topics of hadron physics. PDFs as functions of the longitudinal momentum fraction x can be used to understand the likelihood of finding a quark or a gluon inside a hadron [29]. Through the framework of QCD factorization, they offer a crucial link between the underlying partonic dynamics and cross-sections that can be measured experimentally. Through long-distance components of the cross-section in deep-inelastic scattering (DIS) [30, 31], leading neutron electroproduction [32, 33], prompt photon production [34], J/ψ production [35], and Drell-Yan processes [36], one can extract the PDFs. While significant theoretical and experimental studies are happening for the determination of PDFs for the baryons, particularly the nucleons [37, 38], comparatively less is known about the partonic structure of mesons. Among the mesonic systems, the pion and kaon plays a key role as the lightest quark-antiquark bound state and the pseudo-Goldstone boson associated with the spontaneous breaking of chiral symmetry [3]. In our recent work [39], we have explored the pion PDFs and provided predictions for upcoming EIC experiments. In this study, we extend the PDF calculations for kaons and other heavy pseudoscalar mesons within the light-cone quark model (LCQM).

There have been enough theoretical model predictions [39–42], experimental results [43], theoretical extractions [44–48] and lattice simulation [49, 50] results available for the pion PDFs case compared to the other mesons. It is a challenging task to explore the kaon and other meson PDFs through experimental, however, it is possible to study the PDF behavior of these mesons through theo-

*Electronic address: puhansatyajit@gmail.com

retical models and lattice simulations. For the kaon, the constituent PDFs have been explored in light-front quantization [40], light-front quark model (LFQM) [51], light-front holographic model (LFHM) [52], Dyson-Schwinger equations (DSE) model [53] and chiral quark model [54]. The kaon PDFs have also been investigated within lattice QCD [49, 55] and theoretical extractions [56, 57]. There is only a single dataset available for the kaon-induced Drell-Yan process, four decades ago, by the NA-003 collaboration [58], where it was observed that the softer momentum distribution of the \bar{u} quark in K^- than in π^- . This reflects the suppression of \bar{u} quark in the presence of a heavy s quark, giving rise to the breaking of the SU(3) flavor symmetry. Except for the fixed-target Drell-Yan process, the kaon beam has been used to study J/ψ production in Ref. [59]. The ongoing COMPASS++/AMBER will provide more data for the kaon-induced Drell-Yan process by fixed target experiments using the carbon nucleus $K^- + C \rightarrow \mu^+ \mu^- + X$ [60]. While the upcoming electron-ion collider (EIC) experiments will study the kaon PDFs through the tagged DIS process and Sullivan process ($e + p \rightarrow e' + X + \Lambda$) [61, 62]. It is also difficult to experimentally probe the heavy-meson PDFs due to their very short lifetimes. Heavy mesons provide an ideal platform for testing the interplay between perturbative and non-perturbative QCD due to the heavy flavor content within them. These heavy quark and antiquark constituents move slowly inside the bound state compared to the light mesons. The PDFs of the heavy mesons have been explored in different theoretical models in Refs. [63–68]. Understanding heavy meson PDFs is important for describing hard scattering processes and heavy-flavor production in high-energy collisions, and they play an important role in precision predictions for electroweak boson and Higgs production, as well as collider phenomenology [65].

In this work, we calculate the valence quark and antiquark PDFs of the kaon as well as for the heavy mesons by solving the quark-quark correlation functions in the LCQM. In the case of heavy quarks, the higher Fock-state contributes very little compared to the leading Fock-state [69]. So, for this work, we have only considered the meson state at the lowest Fock-state consists of quark and an antiquark. LCQM is a non-perturbative framework for understanding the internal structure and properties of hadrons, such as mass spectra, radiative decays, decay constants, etc. LCQM is gauge invariant and relativistic by nature. The wave functions of the LCQM are boost invariant in nature. The advantage of LCQM focuses primarily on the valence quarks of hadrons, which are the important constituents responsible for their overall structure and properties. Even after proper QCD evolution of LCQM to the perturbative limit, this model provides excellent results in describing the internal structure. For the case of pseudoscalar mesons, there is only a collinear $f(x)$ PDF available at the leading twist, compared to three for the nucleons. The $f(x)$ is the result of the non-flip quark polarizations inside an unpolarized hadron. By

solving the correlation function, we have derived the PDF in the light-front wave function (LFWF) form and in the explicit form using the total wave function (spin and momentum space wave function). The quark PDF calculated using the leading-order meson Fock-state, for which the gluon and sea-quark contributions vanish at the initial scale. For the heavy mesons, we have considered charm and bottom constituent PDFs present in the B and D -mesons along with quarkonia. For the perturbative QCD calculations, we evolve the initial scale PDFs to higher scales using the next-to-leading (NLO) order Dokshitzer–Gribov–Lipatov–Altarelli–Parisi (DGLAP) evolution equations [70]. The valence, gluon, and sea-quark PDFs are calculated for different mesons at different energy scales along with their Mellin moments. We predict the kaon structure functions as well as the fixed-target Drell-Yan cross-section at NLO. For the kaon cross-section, we have taken Carbon, Aluminum, and Tungsten nuclei as targets from the LHAPDF library [71]. Both K^\pm have been taken into consideration for the calculation of the cross-section. The average momentum fractions carried by the valence, gluon, and sea-quarks has also been predicted for different mesons at different energy scales. We also derive the other higher order Mellin moments at different energy scales. The average momentum fraction of the constituents of the kaon has been compared with other theoretical and lattice QCD predictions. The dominance of the heavy constituent inside the heavy mesons over the lighter constituent has also been studied in this work. The quark-antiquark flavor asymmetry has also been studied for all the mesons at different energy scales. We also study the behavior of the same quark flavors in different mesonic systems at a particular energy scale. This study will provide further insight into the gluon and sea-quark distributions within heavy mesons.

The paper is organized as follows. In Sec. II, we discuss the LCQM, including the spin and momentum wave functions. In Sec. III, we present the results for the quark and antiquark PDFs at the model scale, where the explicit forms of the LFWFs and the Mellin moments are also derived. In this section, we also predict the NLO structure functions and unpolarized Drell-Yan cross-section for the kaon. The flavor asymmetry at the model scale as well as at the higher scales for different mesons have also been derived. Finally, we summarize our findings in Sec. IV.

II. METHODOLOGY

A. Light-cone quark model

The hadron wave function based on the light-front (LF) quantization of QCD using multi-particle Fock-state

expansion is expressed as [1, 11, 21, 72–77]

$$\begin{aligned}
|\Psi_h(P^+, \mathbf{P}_\perp, S_z)\rangle_\Lambda &= \sum_{n, \lambda_i} \int \prod_{i=1}^n \frac{dx_i d^2\mathbf{k}_{\perp i}}{\sqrt{x_i} 16\pi^3} \\
&\times 16\pi^3 \delta\left(1 - \sum_{i=1}^n x_i\right) \delta^{(2)}\left(\sum_{i=1}^n \mathbf{k}_{\perp i}\right) \\
&\times \psi_{n/h}^\Lambda(x_i, \mathbf{k}_{\perp i}, \lambda_i) \\
&\times |n; x_i P^+, x_i \mathbf{P}_\perp + \mathbf{k}_{\perp i}, \lambda_i\rangle. \quad (1)
\end{aligned}$$

Here, $|\Psi_h(P^+, \mathbf{P}_\perp, S_z)\rangle_\Lambda$ is the hadron eigen state with four vector LF momentum $P = (P^+, P_\perp, P^-)$ and spin Λ . S_z is the spin projection of the hadron. For spin-0 pseudoscalar mesons, $S_z = \Lambda = 0$. In the case of $\Lambda = 1$ (vector mesons), S_z will have the values $\pm 1, 0$. x_i and $\mathbf{k}_{\perp i}$ are the longitudinal momentum fraction and transverse momenta of the i^{th} constituent of the hadron. λ_i is the helicity of the i^{th} constituent. The relation among the S_z and λ_i is given as, $S_z = \sum_i \lambda_i + l_z$, where l_z is the orbital angular momentum of the hadron. In the LF dynamics, the momentum and energy of the hadron are distributed among the constituents and obey the conservation rules. The four vector momentum k_i of the i^{th} constituent of the hadron can be expressed as

$$k_i = (k_i^+, \mathbf{k}_{\perp i}, k_i^-) = (x_i P^+, x_i P_\perp + \mathbf{k}_{\perp i}, \frac{\mathbf{k}_{\perp i}^2 + m_i^2}{k_i^+}). \quad (2)$$

Here, m_i is the mass of the i^{th} constituent. The total longitudinal momentum carried by the constituents obeys the momentum conservation rule, $x P^+ = \sum_i^n k_i^+$. This indicates $\sum_i^n x_i = 1$. Similarly, they obey the energy conservation $P^- = \sum_i^n k_i^-$. The transverse momentum of the constituent also obeys the conservation rule: $\sum_i^n \mathbf{k}_{\perp i} = 0$. $\psi_{n/h}^\Lambda(x_i, \mathbf{k}_{\perp i}, \lambda_i)$ in Eq. (1) represents the LF wave function, which appears to be independent of the parent hadron momentum. The hadron eigen state of Eq. (1) obey the normalization condition as

$$\begin{aligned}
&\Lambda \langle \Psi_h(P^{+'}, \mathbf{P}'_\perp, S_z) | \Psi_h(P^+, \mathbf{P}_\perp, S_z) \rangle_\Lambda \\
&= 2(2\pi)^3 P^+ \delta_{\Lambda'\Lambda} \delta(P^+ - P^{+'}) \delta^{(2)}(\mathbf{P}_\perp - \mathbf{P}'_\perp). \quad (3)
\end{aligned}$$

The above formalism of the hadron state is for any composite system, independent of the frame of reference. However, we will describe the meson state, which is the primary goal of this work.

The Fock-state of a meson can be expressed in terms of quarks, gluons, and sea-quark degrees of freedom as [21, 77, 78]

$$\begin{aligned}
|\Psi_m\rangle &= \sum |q\bar{q}\rangle \psi_{q\bar{q}} + \sum |q\bar{q}g\rangle \psi_{q\bar{q}g} + \sum |q\bar{q}gg\rangle \psi_{q\bar{q}gg} \\
&+ \sum |q\bar{q}(q\bar{q})_{\text{sea}}\rangle \psi_{q\bar{q}(q\bar{q})_{\text{sea}}} + \dots \quad (4)
\end{aligned}$$

In LCQM, the Fock-state expansion of mesonic wave functions is reduced to include the lowest Fock-state

solely, for this work. The lowest state's spin-orbit component is regarded as a free state, with quantum numbers including angular momentum, parity, and charge conjugation assigned to the light-front wave functions via the Melosh-Wigner transformation [79]. So in this work, the meson is treated as a Fock-state of the constituent quark-antiquark pair. Now the Eq. (1) can be reduced for a meson eigen state by taking only two particle system $n = 2$ as [21, 76, 80, 81]

$$\begin{aligned}
|\Psi_h(P^+, \mathbf{P}_\perp, S_z)\rangle_\Lambda &= \sum_{\lambda_1, \lambda_2} \int \frac{dx d^2\mathbf{k}_\perp}{\sqrt{x(1-x)} 16\pi^3} \\
&\times \psi_{q\bar{q}}^\Lambda(x, \mathbf{k}_\perp, \lambda_1, \lambda_2) \\
&\times \left| x P^+, \mathbf{k}_\perp, \lambda_1; (1-x) P^+, -\mathbf{k}_\perp, \lambda_2 \right\rangle. \quad (5)
\end{aligned}$$

Here, λ_1 and λ_2 are the helicities of the quark and antiquark, respectively. We will use q for quark and \bar{q} for antiquark throughout this work. The four momenta of the quark (k_q) and antiquark ($k_{\bar{q}}$) are given as

$$k_q \equiv \left(x P^+, \frac{\mathbf{k}_\perp^2 + m_q^2}{x P^+}, \mathbf{k}_\perp \right), \quad (6)$$

$$k_{\bar{q}} \equiv \left((1-x) P^+, \frac{\mathbf{k}_\perp^2 + m_{\bar{q}}^2}{(1-x) P^+}, -\mathbf{k}_\perp \right). \quad (7)$$

$\psi_{q\bar{q}}^\Lambda(x, \mathbf{k}_\perp, \lambda_1, \lambda_2)$ in Eq. (5) is called the momentum space LFWFs, which can be expressed as the combination of radial wave function and spin wave function as [82]

$$\psi_{q\bar{q}}^\Lambda(x, \mathbf{k}_\perp, \lambda_1, \lambda_2) = \phi(x, \mathbf{k}_\perp^2) \mathcal{S}_\Lambda(x, \mathbf{k}_\perp, \lambda_1, \lambda_2), \quad (8)$$

where, $\phi(x, \mathbf{k}_\perp^2)$ and $\mathcal{S}_\Lambda(x, \mathbf{k}_\perp, \lambda_1, \lambda_2)$ are denoted for radial and spin wave functions of the mesons, respectively. For the ground state meson momentum space wave function, we have adopted the BHL prescription [83, 84]. In this prescription, the radial wave function of the mesons is expressed as

$$\begin{aligned}
\phi(x, \mathbf{k}_\perp^2) &= A_h \exp \left[-\frac{\mathbf{k}_\perp^2 + m_q^2}{x} + \frac{\mathbf{k}_\perp^2 + m_{\bar{q}}^2}{1-x} + \frac{m_q^2 + m_{\bar{q}}^2}{4\beta_h^2} \right. \\
&\quad \left. - \frac{(m_q^2 - m_{\bar{q}}^2)^2}{8\beta_h^2 \left(\frac{\mathbf{k}_\perp^2 + m_q^2}{x} + \frac{\mathbf{k}_\perp^2 + m_{\bar{q}}^2}{1-x} \right)} \right], \quad (9)
\end{aligned}$$

for the case of asymmetric quark-antiquark masses [27, 85]. Here, m_q and $m_{\bar{q}}$ are the quark and antiquark masses, respectively. For symmetric quark-antiquark masses ($m_q = m_{\bar{q}}$), the radial wave function is reduced to [79, 86]

$$\phi(x, \mathbf{k}_\perp^2) = A_h \exp \left[-\frac{1}{8\beta_h^2} \frac{\mathbf{k}_\perp^2 + m_{q(\bar{q})}^2}{x(1-x)} + \frac{m_{q(\bar{q})}^2}{2\beta_h^2} \right]. \quad (10)$$

Here, A_h and β_h are the normalization constant and harmonic scale parameters of the respective mesons, respectively. The normalization constant A_h is calculated by normalizing the radial wave function $\phi(x, \mathbf{k}_\perp^2)$ as

$$\int \frac{dx d^2\mathbf{k}_\perp}{2(2\pi)^3} |\phi(x, \mathbf{k}_\perp^2)|^2 = 1. \quad (11)$$

The values of the harmonic scale β_h , quark mass m_q and antiquark mass $m_{\bar{q}}$ used in this work for different mesons have been presented in Table I. These parameters have been taken from our previous work [21, 81], where these parameters are calculated by matching up with meson masses through variational principle [87]. Irrespective of the spin of the mesons, the radial wave function remains the same. But the spin wave function $\mathcal{S}_\Lambda(x, \mathbf{k}_\perp, \lambda_1, \lambda_2)$ mentioned in Eq. (8) is different for mesons with different spins. For this work, we are restricting our calculations to pseudoscalar mesons only ($\Lambda = S_z = 0$). The front-form spin wave function can be derived either from the instant-form by Melosh-Wigner rotation [79, 85] or by solving the quark-meson vertex with proper Dirac spinors. Both methods yield the same spin-wave functions for the spin-0 pseudoscalar mesons. So, in this work, we have considered the spin wave function calculated from the quark-meson vertex as done in our previous works [11, 23, 79, 88, 89]. The spin wave function can be calculated using the proper vertex for spin-0 pseudoscalar mesons ($\Lambda = S_z = 0$) as

$$\begin{aligned} \mathcal{S}(x, \mathbf{k}_\perp, \lambda_1, \lambda_2) &= \bar{u}(k_q, \lambda_1) \\ &\times \frac{\mathcal{A}_{q\bar{q}} \gamma_5}{\sqrt{2(M_{q\bar{q}}^2 - (m_q^2 - m_{\bar{q}}^2))}} v(k_{\bar{q}}, \lambda_2), \end{aligned} \quad (12)$$

with $\mathcal{A}_{q\bar{q}} = M_{q\bar{q}} + m_q + m_{\bar{q}}$. Here, u and v are the light-front Dirac spinors [90]. $M_{q\bar{q}} = \sqrt{\frac{\mathbf{k}_\perp^2 + m_q^2}{x} + \frac{\mathbf{k}_\perp^2 + m_{\bar{q}}^2}{1-x}}$ is the bound state mass of the meson. The spin wave function for pseudoscalar mesons ($S_z = 0$) with different helicity polarizations of quark and antiquark is expressed as [79]

$$\begin{aligned} \mathcal{S}(x, \mathbf{k}_\perp, \uparrow, \uparrow) &= \frac{1}{\sqrt{2}} \omega^{-1}(-\mathbf{k}^L) \mathcal{A}_{q\bar{q}}, \\ \mathcal{S}(x, \mathbf{k}_\perp, \uparrow, \downarrow) &= \frac{1}{\sqrt{2}} \omega^{-1}((1-x)m_q + xm_{\bar{q}}) \mathcal{A}_{q\bar{q}}, \\ \mathcal{S}(x, \mathbf{k}_\perp, \downarrow, \uparrow) &= \frac{1}{\sqrt{2}} \omega^{-1}(-(1-x)m_q - xm_{\bar{q}}) \mathcal{A}_{q\bar{q}}, \\ \mathcal{S}(x, \mathbf{k}_\perp, \downarrow, \downarrow) &= \frac{1}{\sqrt{2}} \omega^{-1}(-\mathbf{k}^R) \mathcal{A}_{q\bar{q}}. \end{aligned} \quad (13)$$

with $\omega = \mathcal{A}_{q\bar{q}} \sqrt{x(1-x)[M_{q\bar{q}}^2 - (m_q - m_{\bar{q}})^2]}$. The above spin wave function obeys the normalization condition

$$\sum_{\lambda_1, \lambda_2} |\mathcal{S}(x, \mathbf{k}_\perp, \lambda_1, \lambda_2)|^2 = 1. \quad (14)$$

Now, finally, the two-particle Fock-state for pseudoscalar mesons in Eq. (5) can be written with all possible helicities of its constituent quark and antiquark, along with the momentum space wave function as

$$\begin{aligned} |\Psi_h(P^+, \mathbf{P}_\perp, S_z = 0)\rangle &= \int \frac{dx d^2\mathbf{k}_\perp}{2(2\pi)^3 \sqrt{x(1-x)}} \phi(x, \mathbf{k}_\perp^2) \\ &\times \left[\mathcal{S}(x, \mathbf{k}_\perp, \uparrow, \uparrow) |xP^+, \mathbf{k}_\perp, \uparrow; (1-x)P^+, -\mathbf{k}_\perp, \uparrow\rangle + \mathcal{S}(x, \mathbf{k}_\perp, \downarrow, \downarrow) |xP^+, \mathbf{k}_\perp, \downarrow; (1-x)P^+, -\mathbf{k}_\perp, \downarrow\rangle \right. \\ &\quad \left. + \mathcal{S}(x, \mathbf{k}_\perp, \downarrow, \uparrow) |xP^+, \mathbf{k}_\perp, \downarrow; (1-x)P^+, -\mathbf{k}_\perp, \uparrow\rangle + \mathcal{S}(x, \mathbf{k}_\perp, \uparrow, \downarrow) |xP^+, \mathbf{k}_\perp, \uparrow; (1-x)P^+, -\mathbf{k}_\perp, \downarrow\rangle \right]. \end{aligned} \quad (15)$$

III. PARTON DISTRIBUTION FUNCTIONS

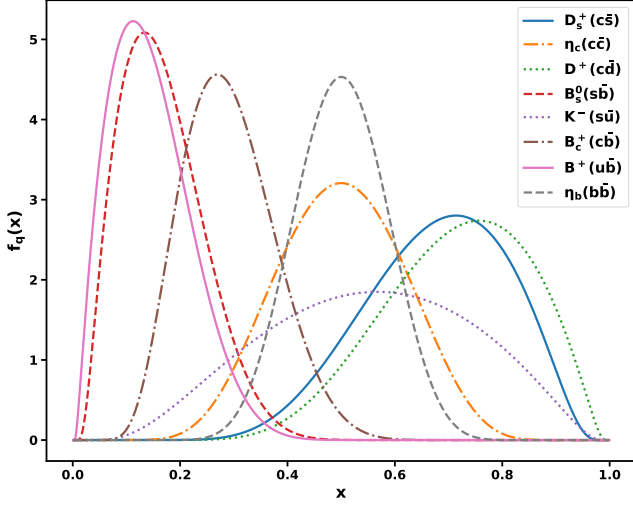
The probability of finding the valence quark-antiquark, gluons and sea-quarks in a meson with the longitudinal momentum degree of freedom can be accessed through the PDFs. For the case of the pseudoscalar mesons, there is only a single unpolarized quark PDF present at the leading twist compared to three for spin- $\frac{1}{2}$ nucleons and four for spin-1 mesons. This unpolarized PDF $f_q(x)$ is the results of the non-flip quark-antiquark helicity polar-

izations within the unpolarized meson. At a fixed light-front time $z^+ = \tau$, the quark-quark correlator of the unpolarized quark PDF is defined as [39, 95]

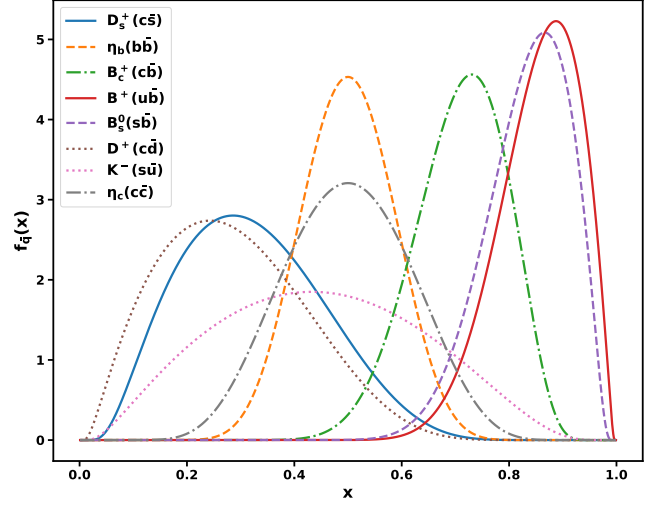
$$\begin{aligned} f_q(x) &= \frac{1}{2} \int \frac{dz^-}{4\pi} e^{ik^+z^-/2} \left\langle \Psi_h(P^+, \mathbf{P}_\perp, S_z = 0) \right| \\ &\quad \left. \bar{\psi}(0) \mathcal{W}(0, z) \Gamma \psi(z) \right| \Psi_h(P^+, \mathbf{P}_\perp, S_z = 0) \rangle \Big|_{z^+, \mathbf{z}_\perp = 0}. \end{aligned} \quad (16)$$

TABLE I: The constituent light quark masses m_q ($q = u, d, s$) and heavy quark masses m_Q ($Q = c, b$), along with the harmonic oscillator scale parameters β_h , are given in units of GeV. These parameters are adopted from Ref. [21, 87].

$m_{u(d)}$	m_s	m_c	m_b	β_{qs}	β_{qc}	β_{cc}	β_{bb}	β_{sc}	β_{qb}	β_{sb}	β_{bc}
0.22	0.45	1.68	5.10	0.405	0.500	0.699	1.376	0.537	0.585	0.636	0.906



(a) (Color online) The quark PDFs $f_q(x)$ of different mesons with respect to x at the initial scales.



(b) (Color online) The antiquark PDFs $f_{\bar{q}}(x)$ of different mesons with respect to x at the initial scales.

FIG. 1: The quark and antiquark PDFs of different mesons as a function x at the initial scale.

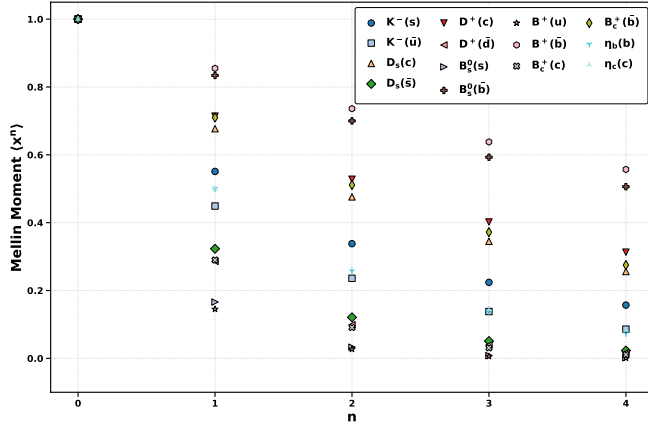


FIG. 2: (Color online) The lower and higher order Mellin moments, $\langle x^n \rangle$, for all quark flavors in different mesons are plotted as functions of n at the initial scale.

Here, $\Gamma = \gamma^+$ is the LF vector current for the unpolarized quark PDFs inside the mesons, which also determines the Lorentz structure of the correlator. $\psi(z)$ is the quark field operator. $z = (z^+, z^-, z_\perp)$ is the position four vector, which is the path of the quark field operators. The Wilson line $\mathcal{W}(0, z)$ preserves the gauge invariance of the bilocal quark field operators in the correlation functions [96] and determines the path of the quark field operators, which has been taken as unity here.

Now using the meson Fock-state of Eq. (15) and quark field operators from Ref. [90], the overlap form of the unpolarized quark PDF $f(x)$ is found to be,

$$f_q(x) = \int \frac{d^2\mathbf{k}_\perp}{16\pi^3} |\phi(x, \mathbf{k}_\perp^2)|^2 \times \left[|\mathcal{S}(x, \mathbf{k}_\perp, \uparrow, \uparrow)|^2 + |\mathcal{S}(x, \mathbf{k}_\perp, \downarrow, \downarrow)|^2 + |\mathcal{S}(x, \mathbf{k}_\perp, \downarrow, \uparrow)|^2 + |\mathcal{S}(x, \mathbf{k}_\perp, \uparrow, \downarrow)|^2 \right]. \quad (17)$$

Now, using the spin wave functions Eq. (13), the explicit form of the quark PDF is found to be

$$f_q(x) = \int \frac{d^2\mathbf{k}_\perp}{16\pi^3} |\phi(x, \mathbf{k}_\perp^2) \mathcal{A}_{q\bar{q}}|^2 \times \frac{\mathbf{k}_\perp^2 + \left((1-x)m_q + xm_{\bar{q}} \right)^2}{\omega^2}. \quad (18)$$

One can obtain the antiquark PDF $f_{\bar{q}}(x)$ by using the momentum sum rule as $f_{\bar{q}}(1-x)$. This indicates that the total longitudinal momentum of the parent meson is totally carried by the quark and antiquark at the initial scale. The unpolarized quark and antiquark PDFs obey

TABLE II: Calculated Mellin moments of the parton distribution functions at the initial scales, $\langle x^n \rangle$ with $n = 0, 1, 2, 3, 4$. For quarkonia states the quark and antiquark moments are identical, while for heavy-light and light-heavy systems they are shown separately.

Meson	Parton	$\langle x^0 \rangle$	$\langle x^1 \rangle$	$\langle x^2 \rangle$	$\langle x^3 \rangle$	$\langle x^4 \rangle$
$K^- (s\bar{u})$	s	1.000	0.551	0.338	0.224	0.157
	\bar{u}	1.000	0.449	0.236	0.138	0.0861
$D_s (c\bar{s})$	c	1.000	0.677	0.476	0.345	0.256
	\bar{s}	1.000	0.323	0.121	0.051	0.023
$D^+ (c\bar{d})$	c	1.000	0.714	0.528	0.402	0.313
	\bar{d}	1.000	0.286	0.099	0.039	0.017
$B_s^0 (s\bar{b})$	s	1.000	0.166	0.033	0.008	0.002
	\bar{b}	1.000	0.834	0.700	0.593	0.506
$B^+ (u\bar{b})$	u	1.000	0.145	0.027	0.006	0.001
	\bar{b}	1.000	0.855	0.736	0.638	0.557
$B_c^+ (c\bar{b})$	c	1.000	0.290	0.091	0.031	0.011
	\bar{b}	1.000	0.710	0.511	0.372	0.275
$\eta_b (b\bar{b})$	b/\bar{b}	1.000	0.500	0.257	0.136	0.073
$\eta_c (c\bar{c})$	c/\bar{c}	1.000	0.500	0.263	0.145	0.083

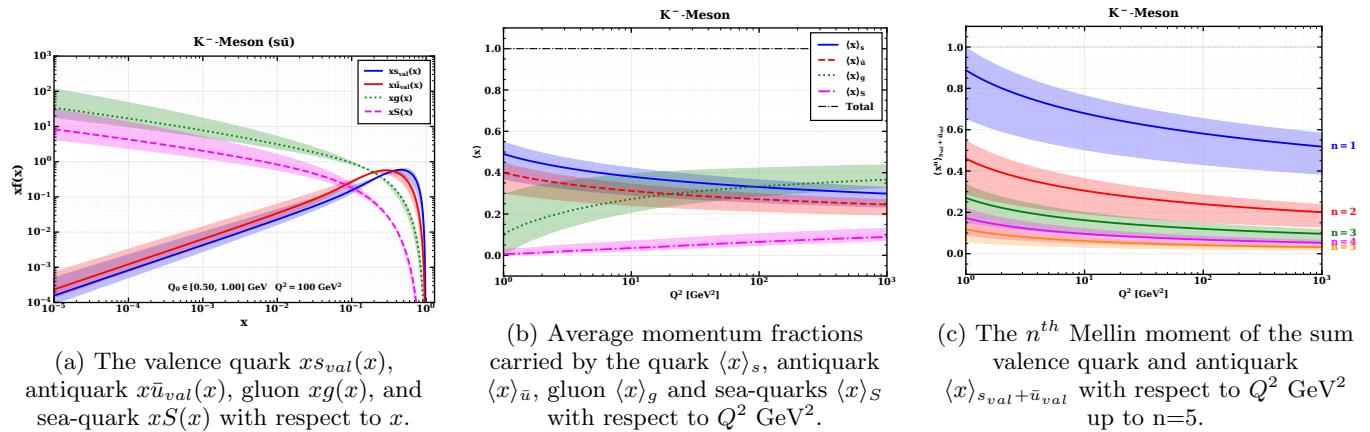


FIG. 3: (Color online) The $K^- (s\bar{u})$ -meson PDFs have been evolved to $Q^2 = 100$ GeV² through NLO DGLAP evolutions by taking the initial scale $Q_0 \in [0.50, 1.00]$ GeV. The central line corresponds to the initial scale $Q_0 = 0.75$ GeV.

TABLE III: Initial scale Q_0 values used in this work for different mesons.

Mesons	Q_0 [GeV]
K^-	0.50–1.00
D^+, D_s, η_c	1.68–3.36
B_s^0, B_c, η_b, B^+	5.10–10.20

the PDF sum rule [21, 22]

$$\begin{aligned}
 \int_0^1 dx f_q(x, Q_0^2) &= 1, \\
 \int_0^1 dx f_{\bar{q}}(x, Q_0^2) &= 1, \\
 \int_0^1 dx x [f_q(x, Q_0^2) + \bar{f}_{\bar{q}}(x, Q_0^2)] &= 1.
 \end{aligned} \tag{19}$$

As, we have not consider the gluon and sea-quark contributions in this work at the initial scale, so both of them

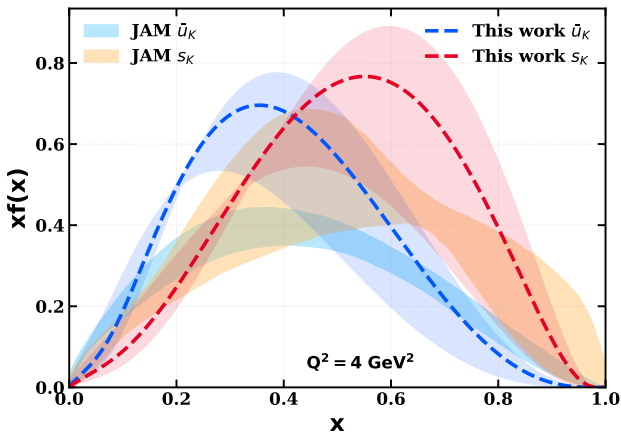


FIG. 4: (Color online) The evolved quark and antiquark PDFs of kaon have been compared with recent JAM results at $Q^2 = 4 \text{ GeV}^2$ [55]. The error band corresponds to the initial scale ranges $Q_0 \in [0.5, 1.0] \text{ GeV}$.

are zero as

$$\begin{aligned} \int_0^1 dx g(x, Q_0^2) &= 0, \\ \int_0^1 dx S(x, Q_0^2) &= 0. \end{aligned} \quad (20)$$

Here, g and S represent the gluon and sea-quark contributions, respectively. It is important to note that Q_0 corresponds to the lower limit of the initial scale range considered in this work. The dynamical gluon contributions arising from higher Fock states for the pion and kaon are currently under investigation, and the corresponding results will be reported in a future work.

A. Initial Scale PDFs

For this work, we have considered all the ground state pseudoscalar mesons from our previous work [81] for a complete description of quark and antiquark inside the different mesonic systems. We have considered the $K^-(s\bar{u})$, D-mesons ($D^+(c\bar{d})$ and $D_s^+(c\bar{s})$), charmonia $\eta_c(c\bar{c})$, bottomonia $\eta_b(b\bar{b})$ and B-mesons ($B^+(u\bar{b})$, $B_c^+(c\bar{b})$ and $B_s^0(s\bar{b})$). A detailed study of the pion PDF using LCQM has been reported in our previous work [39]. The kaon PDFs are among the central goals of the COMPASS/AMBER program in the kaon-induced Drell-Yan process at JLab, along with upcoming EIC experiments. However, it is challenging to extract the other mesons PDFs directly from the experiments due to their very short lifetimes. For the numerical calculations, we need only two parameters quark-antiquark masses $m_{q(\bar{q})}$ and harmonic scale parameter β_h , which have been shown in the Table. I. The initial quark and antiquark PDFs

have been presented as a function of longitudinal momentum fraction (x) in Fig. 1. All the quark and antiquark PDFs are found to have positive distributions over the entire x -region. The antiquark PDFs are found to have widths and peak distributions similar to those of the quark PDFs. The mesons with symmetric quark-antiquark mass (charmonia and bottomonia) are found to have symmetric behavior of PDFs around $x = 0.5$. For the heavy quark and light antiquark mass (kaon and D-mesons), the PDFs are found to have maximum distributions in the region $x \geq 0.5$. While looking into B-mesons, which have light quark and heavy antiquark masses, the PDFs are found to have maximum distributions in the range $0 \leq x \leq 0.5$. The width of the spread of the quark PDFs is found to mainly depend on the meson mass. Mesons with higher mass are found to have lower widths, and vice versa. From Fig. 1 (a), it is observed that the quark PDF of the heavy η_b -meson ($b\bar{b}$) has a lesser width compared to the η_c -meson. Overall, the valence quark and antiquark PDFs of the B^+ -meson found have a lesser spread compared to all other PDFs. It is also observed that the peak of the quark PDFs is dependent on the meson mass. Higher the mass of the mesons, higher is the peak of distributions. This kind of behavior is expected for the heavier meson mass case, as the running coupling is smaller, which leads to the smaller kinetic energy of the system. Thus, the probability of carrying small longitudinal momentum by the quark and antiquark in heavier mesons is always small, and the peak distribution is higher. The smaller running coupling value makes the system non-relativistic in nature compared to the light mesons. So, in a certain region of x , the quark and antiquark PDFs are found to be zero for heavy mesons. Similar kind of results have been also reported in BLFQ [65], Bethe-Salpeter wave functions (BSWFs) [69, 97], LFQM [63, 98], holographic basis [66, 99–101] and in Ref. [102].

We have also calculated the lower and higher order Mellin moments $\langle x^n \rangle$ of the quark and antiquark PDFs of different meson, which can be computed as

$$\langle x^n \rangle = \frac{\int dx x^n f(x, Q^2)}{\int dx f(x, Q^2)}. \quad (21)$$

The n^{th} Mellin moments of the quark and antiquark PDFs of different mesons at the initial scale Q_0 have been presented in the Table II. At $n = 0$, the Mellin moment provides the information about the number of valence quarks, which is found to be 1 for each flavor. While for $n = 1$, which tells us about the average momentum fraction carried by the constituent quark and antiquark within the mesonic systems. The total momentum fraction carried by quark and antiquark obeys the sum rule of Eq. (19) at the model scale. We have also represented the Mellin moment of different quark-antiquark flavors of different mesons in the Fig. 2. In the Table. II and Fig. 2, it is observed that the momentum fraction carried by the heavy constituent is higher

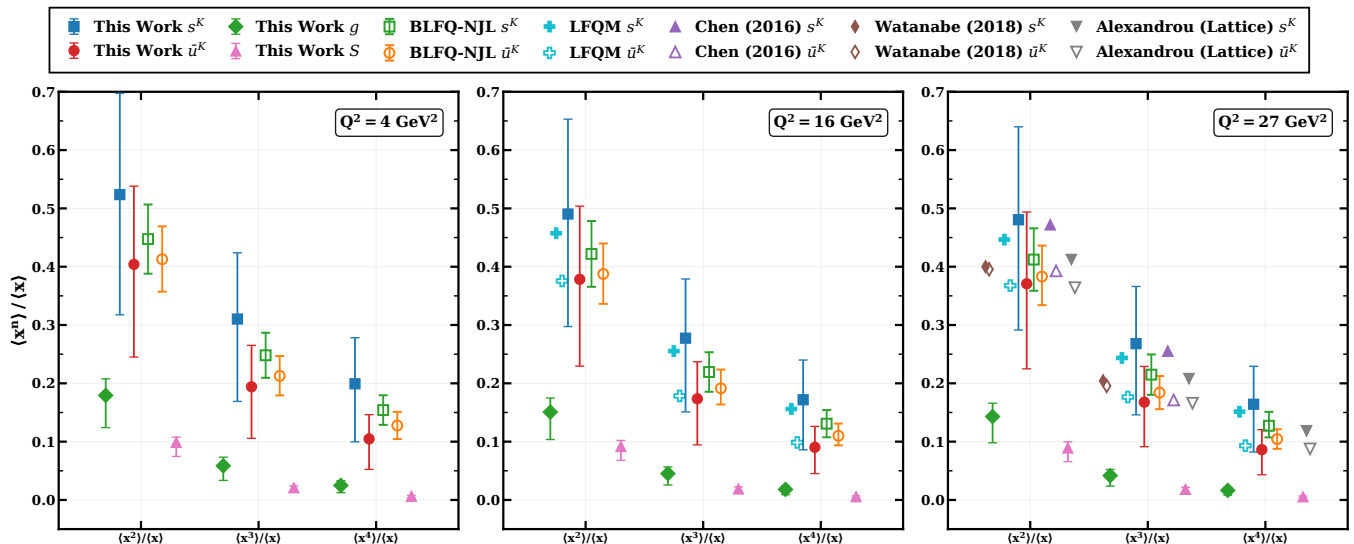


FIG. 5: (Color online) The Mellin moment ratio of $\langle x^n \rangle / \langle x \rangle$ of valence, gluon and sea-quark PDFs of the kaon have been plotted at different energy scales $Q^2 = 4, 16$ and 27 GeV^2 . We have also compared our results with available theoretical models [40, 51, 91, 92] and lattice simulation [93] results.

TABLE IV: First and second Mellin moments of the valence quark, antiquark, gluon and sea-quarks K^- -meson at $Q^2 = 4, 16$ and 27 GeV^2 scales. The uncertainties correspond to the variation of the initial scale $Q_0 \in [0.50, 1.00] \text{ GeV}$.

Q^2 (GeV^2)	Moment	$\langle x^n \rangle_{s_{\text{val}}}$	$\langle x^n \rangle_{\bar{u}_{\text{val}}}$	$\langle x^n \rangle_g$	$\langle x^n \rangle_{\text{sea}}$
4	$\langle x \rangle$	$0.428^{+0.054}_{-0.114}$	$0.312^{+0.039}_{-0.083}$	$0.236^{+0.130}_{-0.209}$	$0.024^{+0.037}_{-0.012}$
	$\langle x^2 \rangle$	$0.231^{+0.046}_{-0.086}$	$0.133^{+0.026}_{-0.049}$	$0.043^{+0.006}_{-0.010}$	$0.0025^{+0.0023}_{-0.0011}$
16	$\langle x \rangle$	$0.378^{+0.048}_{-0.101}$	$0.276^{+0.035}_{-0.073}$	$0.305^{+0.124}_{-0.189}$	$0.041^{+0.041}_{-0.015}$
	$\langle x^2 \rangle$	$0.192^{+0.038}_{-0.071}$	$0.110^{+0.022}_{-0.041}$	$0.046^{+0.001}_{-0.004}$	$0.0039^{+0.0019}_{-0.0011}$
27	$\langle x \rangle$	$0.364^{+0.046}_{-0.097}$	$0.266^{+0.034}_{-0.071}$	$0.322^{+0.122}_{-0.184}$	$0.048^{+0.042}_{-0.016}$
	$\langle x^2 \rangle$	$0.181^{+0.036}_{-0.067}$	$0.104^{+0.021}_{-0.039}$	$0.046^{+0.000}_{-0.003}$	$0.0045^{+0.0017}_{-0.0011}$

compared to the lighter constituent within a particular meson. In this work, the longitudinal momentum fraction of the constituent is found to obey the relations

$$\langle x \rangle_{q(\bar{q})} \propto m_{q(\bar{q})}. \quad (22)$$

The bottom antiquark PDFs of B-mesons are found to carry a higher longitudinal momentum fraction than those of other flavors, as observed in Fig. 2. The difference in the momentum fraction carried by the quark and antiquark ($\langle x \rangle_q - \langle x \rangle_{\bar{q}}$) of a particular meson is also found to depend upon the mass difference of the quark and antiquark of the mesons. The B-mesons, having a large difference in quark and antiquark masses, are found to have a higher $\langle x \rangle_q - \langle x \rangle_{\bar{q}}$ value compared to the other mesons at the initial scale. While for the case of mesons having symmetric quark-antiquark mass, both the constituents are found to carry equal momentum fractions. In Fig. 2, it is also observed that the suppression of the properties of the light quark occurs in the presence of the

heavy quark inside the meson. The Mellin moment $\langle x^n \rangle$ carried by the u, s, c and b flavors in the different mesons is found to follow the order at the initial scale as

$$\begin{aligned} \langle x^n \rangle_u^{K^-} &> \langle x^n \rangle_u^{B^+}, \\ \langle x^n \rangle_s^{K^-} &> \langle x^n \rangle_s^{D_s^+} > \langle x^n \rangle_s^{B_s^0}, \\ \langle x^n \rangle_c^{D^+} &> \langle x^n \rangle_c^{D_s^+} > \langle x^n \rangle_c^{\eta_c} > \langle x^n \rangle_c^{B_c^+}, \\ \langle x^n \rangle_b^{B^+} &> \langle x^n \rangle_b^{B_s^0} > \langle x^n \rangle_b^{B_c^+} > \langle x^n \rangle_b^{\eta_b}. \end{aligned} \quad (23)$$

Understanding the PDFs in non-perturbative models is crucial for the hadrons intrinsic structure at low energy scales. However, this alone is inadequate for important phenomenological use. Perturbative QCD evolution equations must be used to evolve these model-generated PDFs to higher momentum scales in order to permit reliable comparisons with existing experimental results and to make reliable predictions for future high-energy investigations. The perturbative regime investigated in deep

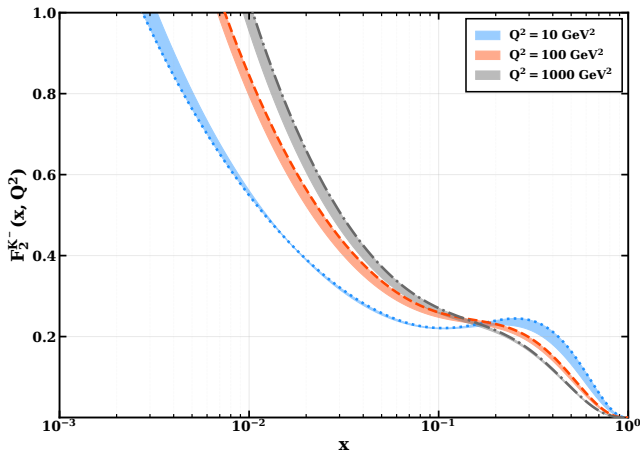


FIG. 6: (Color online) The $F_2^{K^-}$ structure functions of the kaon have been predicted at $Q^2 = 10, 100$ and 1000 GeV^2 at NLO by taking the initial scale range of $Q_0 \in [0.5, 1.0]$ GeV .

inelastic scattering and collider operations is linked to the non-perturbative dynamics controlling hadron structure at low scales through this scale evolution. These evolutions have been carried out through standard DGLAP evolution using the HOPPET toolkit at NLO accuracy throughout this work [103].

The DGLAP equation, which bridges PDFs between a final scale and an initial scale is given by [31, 104–106]

$$\frac{\partial f(x, Q^2)}{\partial \ln Q^2} = \frac{\alpha_s(Q^2)}{2\pi} [P_{qq} \otimes q + P_{qg} \otimes g], \quad (24)$$

$$\frac{\partial g(x, Q^2)}{\partial \ln Q^2} = \frac{\alpha_s(Q^2)}{2\pi} [P_{gq} \otimes q + P_{gg} \otimes g], \quad (25)$$

with

$$(P \otimes f)(x) = \int_x^1 \frac{dz}{z} P\left(\frac{x}{z}\right) f(z, Q^2). \quad (26)$$

Here, $\alpha_s(Q^2)$ is the strong coupling constant, which has been taken directly from LHAPDF library of CT14 proton PDF at particular Q^2 values [71]. z is the momentum fraction of the parent parton before the splitting. P_{qq} , P_{qg} , P_{gq} , and P_{gg} are the fundamental splitting kernel appearing in the DGLAP equations. The valence PDFs obtained from LCQM will start radiating into gluons, further the gluons split into sea-quarks with an increase in energy scales. So, from non-perturbative quark PDFs, one can obtain the higher scale valence, gluon and sea-quark PDFs of different mesons.

B. Evolved Constituent PDFs

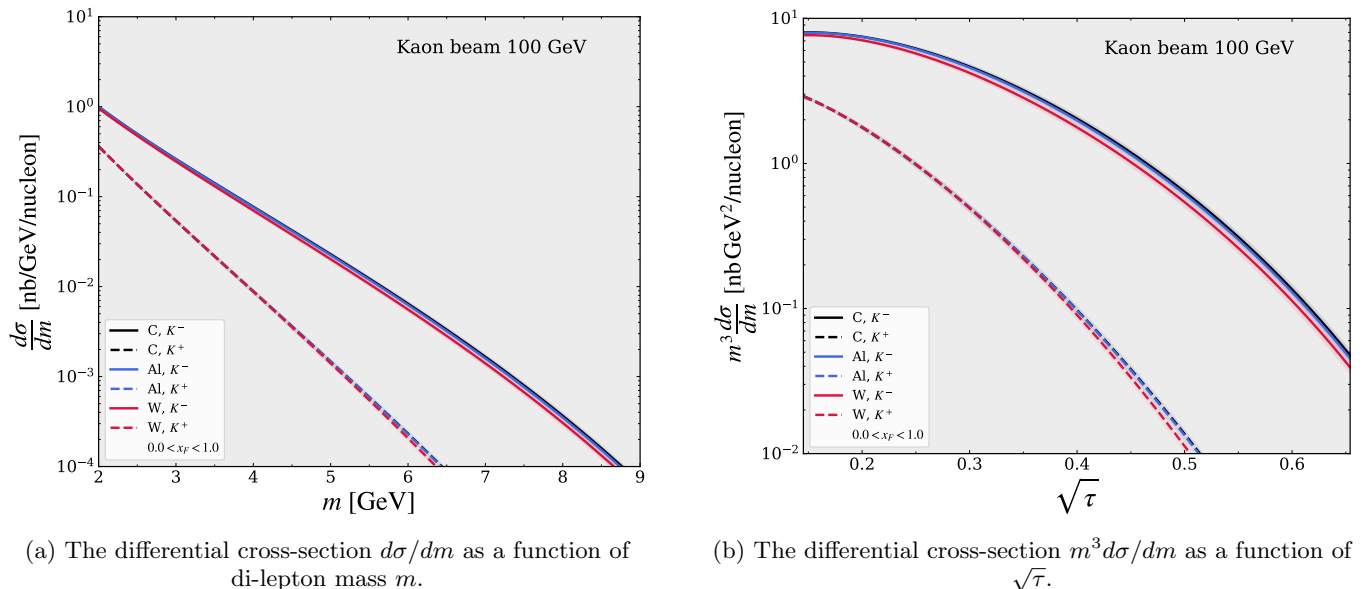
The quark and antiquark PDFs, presented in Fig. 1 for different mesons have been evolved to higher energy

scales by taking the initial scale range from Q_0 to $2Q_0$ using the NLO DGLAP evolutions. The corresponding initial scales for different mesons are presented in the Table. III. The initial scale for different mesons has been chosen as $Q_0 \geq m_Q$ (here m_Q is the mass of the heavy constituent inside the mesonic system). This choice ensures that the scale is sufficiently large to support a meaningful partonic description in terms of valence quark and antiquark distributions.

Among all the mesons considered, the kaon still can be treated as a light meson after the pion, consisting of a light up and heavy strange quark-antiquark pair. These valence quark and antiquark PDFs have been evolved to a higher energy scale of $Q^2 = 100$ GeV^2 by taking the initial scale range $Q_0 = 0.50$ GeV and have been presented in Fig. 3. The error band in the valence, gluon and sea-quark PDFs corresponds to the initial scale range from Q_0 to $2Q_0$. In Fig. 3 (a), we observed that the valence antiquark is found to have slightly higher distributions compared to the quark PDFs at the high x region. While the gluon and sea-quark PDFs are found to dominate in the low x region. In Figs. 3 (b) and 3 (c), we have plotted the lower and higher Mellin moments of the constituent of the kaon by taking the energy scale range from $1 \leq Q^2 \leq 10^3$ GeV^2 . The valence antiquark PDF is found to carry a higher longitudinal momentum fraction compared to the valence quark PDF. The momentum fraction of the gluon and sea-quark is found to increase with an increase in energy scales Q^2 due to the quark-antiquark splittings. At any energy scale Q^2 , the constituents obey the momentum sum rule of

$$\int_0^1 dx x \left[f_{\text{val}}(x, Q^2) + \bar{f}_{\text{val}}(x, Q^2) + S(x, Q^2) + g(x, Q^2) \right] = 1. \quad (27)$$

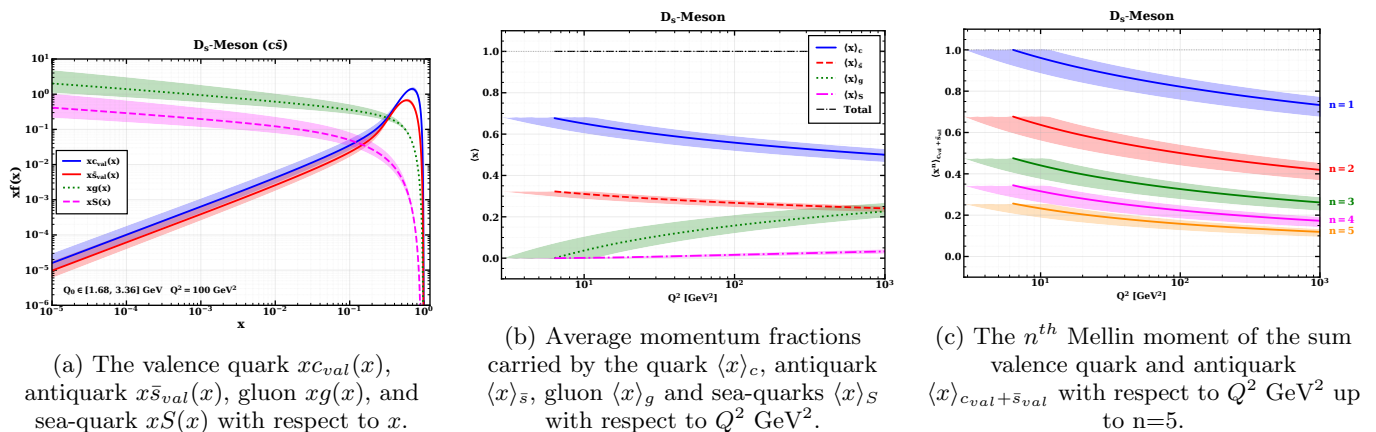
The higher order Mellin moments up to $n = 4$ of the total valence PDFs have been plotted in Fig. 3 (c), which are found to be gradually decreasing with an increase in energy scales. There is no experimental data available for the kaon PDFs till now, however a few lattice simulation results are available for these PDFs [49, 55]. The evolved quark and antiquark PDFs of the kaon have been compared with the recent JAM PDFs in Fig. 4 at the energy scale $Q^2 = 4$ GeV^2 by taking the initial scale range in our work. The PDFs are found to be consistent with the JAM results in the high- x region [55], while deviating in the mid- x region. However, due to the initial scale range, the evolved PDFs are found to have a higher distribution than other extraction results [57] and lattice simulation results [49]. We have also predicted the calculated Mellin moment for different constituent of the kaon in the Table. IV up to $n = 2$. Our valence constituents are found to carry higher longitudinal momentum fraction than the available theoretical and lattice QCD results [40, 51, 91–93]. The higher order Mellin moment ratio $\langle x^n \rangle / \langle x \rangle$ of valence, gluon and sea-quark PDFs of the kaon have been



(a) The differential cross-section $d\sigma/dm$ as a function of di-lepton mass m .

(b) The differential cross-section $m^3 d\sigma/dm$ as a function of $\sqrt{\tau}$.

FIG. 7: (Color online) The differential cross-section for the kaon induced DY process by taking different target nucleus of Carbon (C), Aluminum (Al) and Tungsten (W). The nuclear PDFs have been taken from CTEQ15 datasets [94].



(a) The valence quark $x c_{val}(x)$, antiquark $x \bar{s}_{val}(x)$, gluon $x g(x)$, and sea-quark $x S(x)$ with respect to x .

(b) Average momentum fractions carried by the quark $\langle x \rangle_c$, antiquark $\langle x \rangle_{\bar{s}}$, gluon $\langle x \rangle_g$ and sea-quarks $\langle x \rangle_S$ with respect to Q^2 GeV².

(c) The n^{th} Mellin moment of the sum valence quark and antiquark $\langle x \rangle_{c_{val} + \bar{s}_{val}}$ with respect to Q^2 GeV² up to $n=5$.

FIG. 8: The $D_s(c\bar{s})$ -meson PDFs have been evolved to $Q^2 = 100$ GeV² through NLO DGLAP evolutions by taking the initial scale $Q_0 \in [1.68, 3.36]$ GeV. The central line corresponds to the initial scale $Q_0 = 2.52$ GeV.

plotted at different energy scales $Q^2 = 4, 16$ and 27 GeV² in Fig. 5. These Mellin moment ratios are found to have consistent values when compared with variable theoretical models [40, 51, 91, 92] and lattice simulation [93] results. Due to the initial scale range, our results have larger error bars than those of the others. We have also predicted the kaon structure functions for the upcoming EIC experiments at the NLO accuracy. The kaon structure function at NLO can be calculated by taking the

total quark and gluon distributions as

$$F_2(x, Q^2) = \sum_q e_q^2 x \left\{ f_q(x, Q^2) + f_{\bar{q}}(x, Q^2) + \frac{\alpha_s(Q^2)}{2\pi} \times \left[C_{2q}[z] \otimes (f_q(x, Q^2) + f_{\bar{q}}(x, Q^2)) + 2 C_{2g}[z] \otimes g(x, Q^2) \right] \right\}, \quad (28)$$

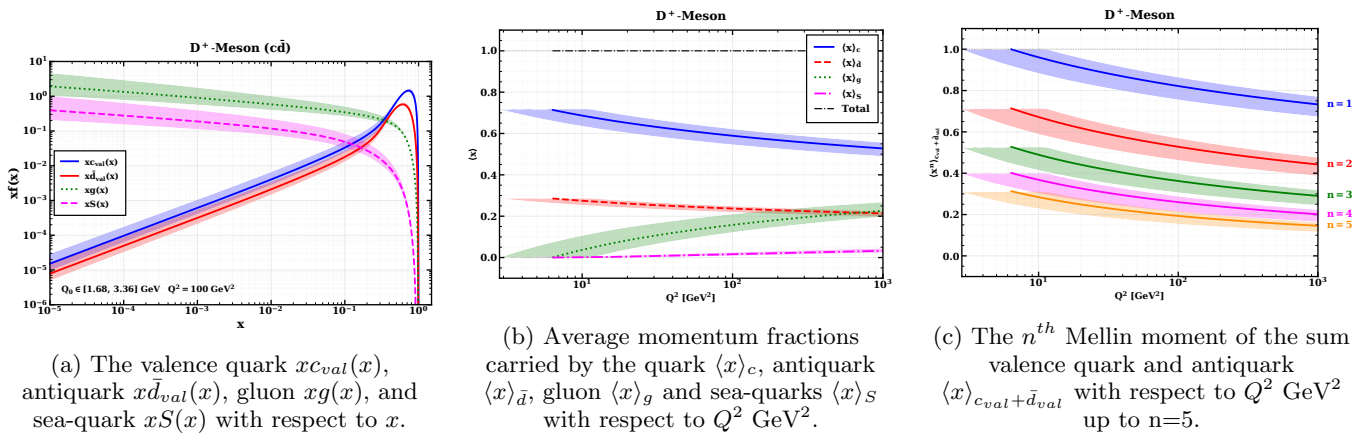


FIG. 9: (Color online) The $D^+(c\bar{d})$ -meson PDFs have been evolved to $Q^2 = 100$ GeV² through NLO DGLAP evolutions by taking the initial scale $Q_0 \in [1.68, 3.36]$ GeV. The central line corresponds to the initial scale $Q_0 = 2.52$ GeV.

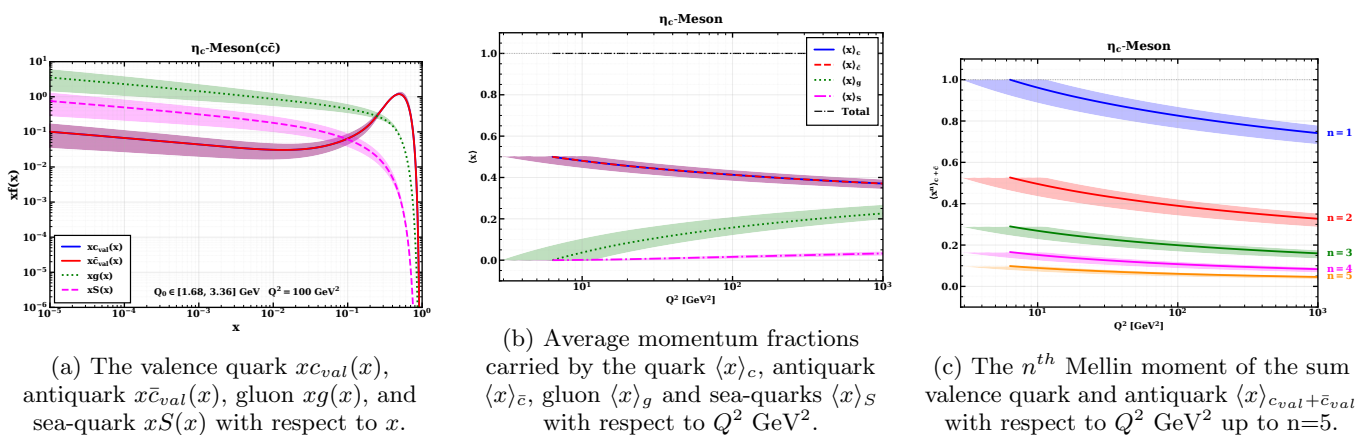


FIG. 10: (Color online) The $\eta_c(c\bar{c})$ -meson PDFs have been evolved to $Q^2 = 100$ GeV² through NLO DGLAP evolutions by taking the initial scale $Q_0 \in [1.68, 3.36]$ GeV. The central line corresponds to the initial scale $Q_0 = 2.52$ GeV.

with the $\overline{\text{MS}}$ scheme

$$C_{2q}^{\overline{\text{MS}}}(z) = C_F \left[2 \left(\frac{\ln(1-z)}{1-z} \right)_+ - \frac{3}{2} \left(\frac{1}{1-z} \right)_+ - (1+z) \ln(1-z) - \frac{1+z^2}{1-z} \ln z \right. \\ \left. + 3 + 2z - \left(\frac{\pi^2}{3} + \frac{9}{2} \right) \delta(1-z) \right], \quad (29)$$

$$C_{2g}^{\overline{\text{MS}}}(z) = T_R \left[\left((1-z)^2 + z^2 \right) \ln \left(\frac{1-z}{z} \right) - 8z^2 + 8z - 1 \right]. \quad (30)$$

Here, $C_F = 4/3$ and $T_R = 1/2$ are the color factors. In Fig. 6, we have plotted the kaon structure functions as

a function of x at energy scales $Q^2 = 10, 100$ and 1000 GeV². The distribution of the structure function of the kaon is found to increase in the region $x \leq 0.05$ with an increase in Q^2 , while vice versa in the region $x \geq 0.05$. This is mainly due to the splitting of the valence quark-antiquark into gluon and sea-quark with an increase in energy scales. One important thing to note is that the upcoming EIC experiments will study kaon structure using the Sullivan process via a complex Tagged Deep Inelastic Scattering (TDIS) process [107]. We have also predicted the differential cross-section for the kaon induced fixed target Drell-Yan process ($K^\pm + A \rightarrow \ell^+ \ell^- + X$) for the upcoming COMPASS++/AMBER experiment at CERN. The COMPASS will measure the Drell-Yan cross-section of a kaon beam striking a carbon target, which contains equal numbers of protons and neutrons, aiming to explore the structure of the kaon [60]. Here, we have predicted the Drell-Yan cross-section by using the fixed-target nuclear PDFs for carbon (C), Aluminum (Al)

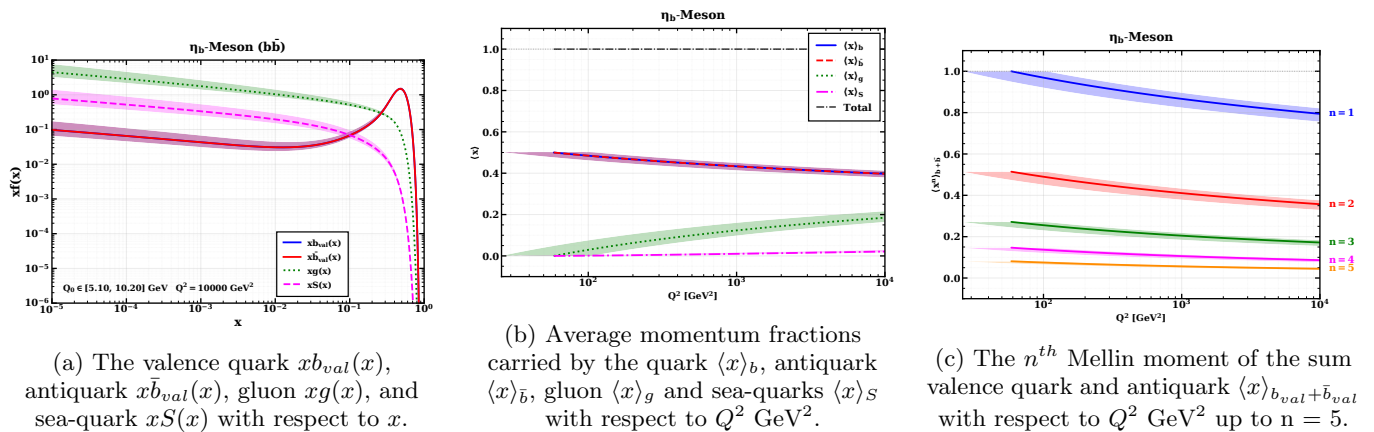


FIG. 11: (Color online) The $\eta_b(b\bar{b})$ -meson PDFs have been evolved to $Q^2 = 1000$ GeV² through NLO DGLAP evolutions by taking the initial scale $Q_0 \in [5.10, 10.20]$ GeV. The central line corresponds to the initial scale $Q_0 = 7.65$ GeV.

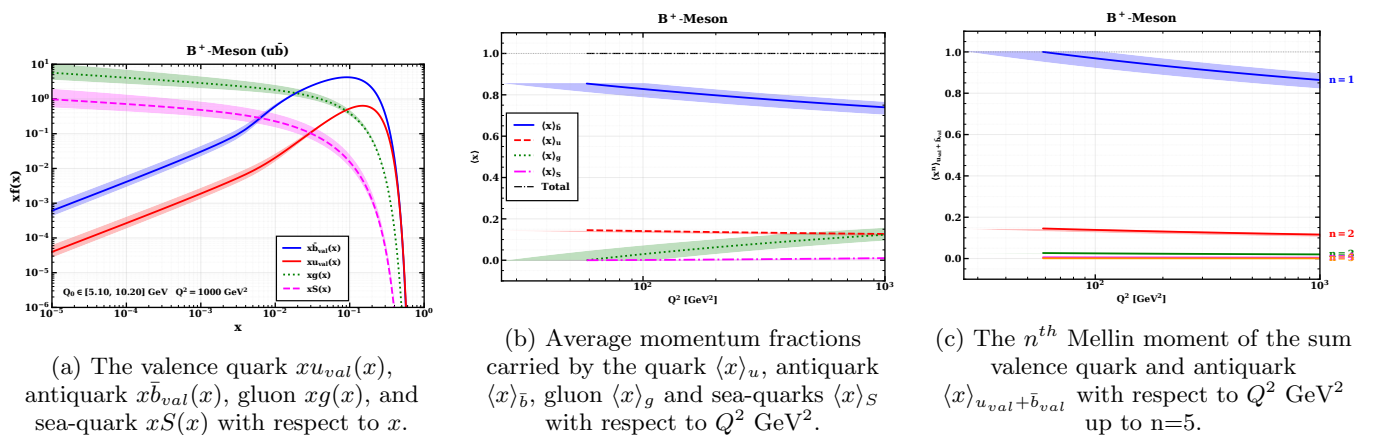


FIG. 12: (Color online) The $B^+(u\bar{b})$ -meson PDFs have been evolved to $Q^2 = 1000$ GeV² through NLO DGLAP evolutions by taking the initial scale $Q_0 \in [5.10, 10.20]$ GeV. The central line corresponds to the initial scale $Q_0 = 7.65$ GeV.

and Tungsten (W) from the CTEQ15 datasets [94]. The differential cross-section of the kaon-induced Drell-Yan process in terms of the target nucleus and incoming kaon PDFs at NLO can be expressed as [39, 40, 108]

$$\frac{m^3 d^2\sigma}{dm dY} = \frac{8\pi\alpha_s^2(Q^2)}{9} \frac{m^2}{s} \sum_{ij} \int dx_1 dx_2 \times C_{ij}(x_1, x_2, s, m, Q^2) f_{i/K}(x_1, Q^2) f_{j/A}(x_2, Q^2), \quad (31)$$

where C_{ij} is the hard-scattering kernels, which are expanded using the powers of the strong coupling constant α_s as

$$C_{ij}(x_1, x_2, s, m, Q^2) = \sum_{n=0}^{\infty} \left(\frac{\alpha_s}{2\pi}\right)^n C_{ij}^{(n)}(x_1, x_2, s, m, Q^2). \quad (32)$$

The form of C_{ij} at NLO has been taken from the Ref.

[108]. The sum includes the $q\bar{q}$ annihilation channels, as well as quark-gluon (qg) and antiquark-gluon ($\bar{q}g$). Here, $f_{i/\pi}(x_1, Q^2 = m^2)$ is the final evolved PDF and $f_{j/A}(x_2, Q^2)$ is the nuclear PDFs. By integrating over the rapidity Y , we have predicted the differential Drell-Yan cross-section and have plotted it in Fig. 7. In Figs. 7 (a) and 7 (b), we have plotted the $d\sigma/dm$ as a function of di-lepton mass m and $m^3 d\sigma/dm$ as a function of $\sqrt{\tau}$, respectively. For a better understanding, we have also considered both $K^+(u\bar{s})$ and $K^-(s\bar{u})$ mesons at the same beam energy of 100 GeV. The K^- cross-section is found to have a higher distribution compared to the K^+ , which was also observed in the kaon-induced J/ψ production experiment [59]. The calculated cross-sections for both mesons also show a distribution similar to that predicted by recent BLFQ [109]. The different nuclear PDFs are found to have a lesser effect on the total cross-section of the kaon. The cross-section ratio $\frac{\sigma(K^+)}{\sigma(K^-)}$ in this

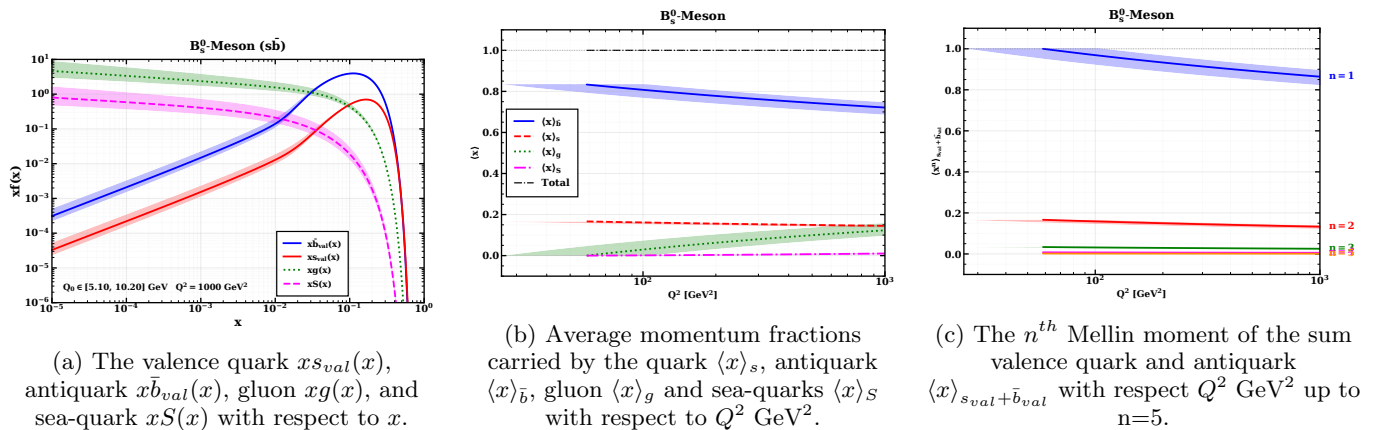


FIG. 13: (Color online) The $B_s^0(s\bar{b})$ -meson PDFs have been evolved to $Q^2 = 1000$ GeV² through NLO DGLAP evolutions by taking the initial scale $Q_0 \in [5.10, 10.20]$ GeV. The central line corresponds to the initial scale $Q_0 = 7.65$ GeV.

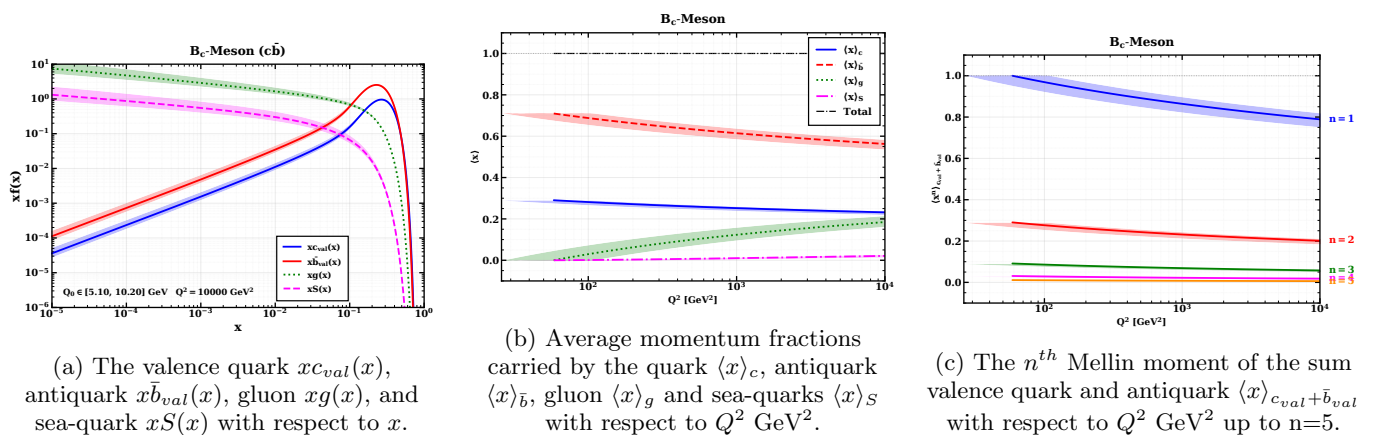


FIG. 14: (Color online) The $B_c(c\bar{b})$ -meson PDFs have been evolved to $Q^2 = 1000$ GeV² through NLO DGLAP evolutions by taking the initial scale $Q_0 \in [5.10, 10.20]$ GeV. The central line corresponds to the initial scale $Q_0 = 7.65$ GeV.

work is found to be 0.28 ± 0.012 compared J/ψ production results of 0.29 ± 0.07 [59]. Further experimental data are required in the kaon sector to validate these results.

Except for the kaon, accessing the internal structure of other heavy mesons considered in this work remains challenging. Nonetheless, investigating their PDFs is crucial for describing processes such as heavy-ion collisions, quarkonium production, and exclusive and inclusive hadronic reactions, where non-perturbative QCD effects are significant. So, in this study, we have demonstrated the PDFs for the range $x \geq 10^{-5}$ with the energy scales relevant to the Electron-Ion-Collider in China (EicC) [110], the electron-Relativistic Heavy Ion Collider (eRHIC) [111] and the Large Hadron Electron Collider (LHeC) experiments [112]. In Figs. 8 and 9, we have plotted the behavior of the evolved valence PDFs of the $D_s(c\bar{s})$ and $D^+(c\bar{d})$ -mesons to a higher scale of $Q^2 = 100$ GeV² by taking an initial scale range of $Q_0 = m_c$ to $2m_c$. The heavy c -quark of the mesons is found to have

a higher distribution compared to the light constituent and also carries a higher longitudinal momentum fraction than others. Compared to the kaon, the gluon and sea-quark distributions are found to be lower for these mesons. This behavior indicates reduced gluon radiation and suppressed sea-quark generation in heavy-light mesons, arising from the large charm quark mass and the shorter DGLAP evolution length. This behavior is also seen in Figs. 8 (c) and 9 (c), where the total momentum fraction carried by the valence PDFs is decreasing slowly compared to the kaon case. The momentum fraction of the valence PDFs is found to decrease by almost 25% from the initial scale Q_0 . A similar pattern is also observed for the higher Mellin moments. In Fig. 10, we have presented the constituent PDFs of the heavy quarkonium state $\eta_c(c\bar{c})$ at the scale $Q^2 = 100$ GeV², evolved from an initial scale range $Q_0 \in [1.68, 3.36]$ GeV. For quarkonium systems, it is not possible to distinguish sea antiquarks from valence quarks due to the identical flavor

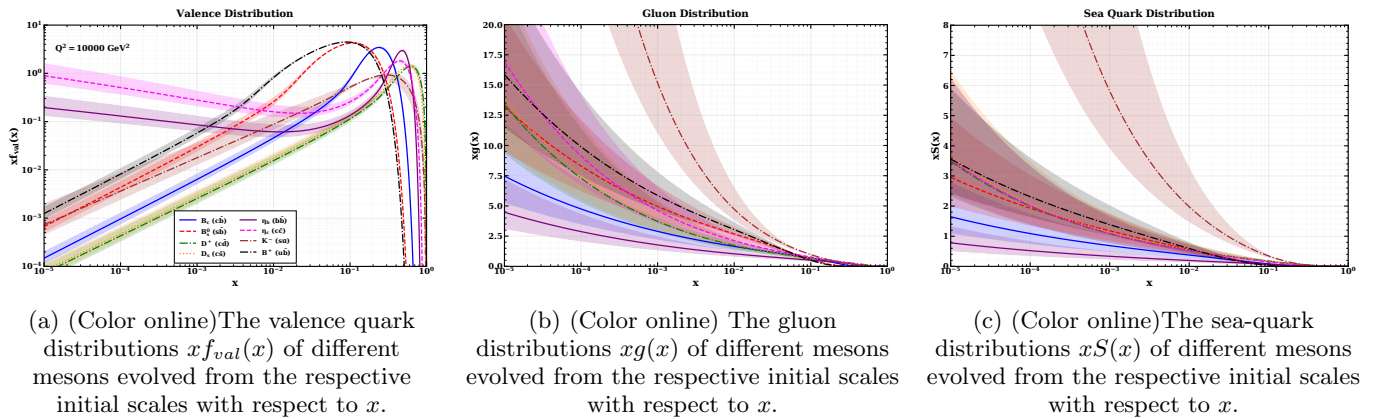


FIG. 15: (Color online) The constituent PDFs of all the mesons have been evolved to $Q^2 = 10000 \text{ GeV}^2$ by taking the respective initial scales as given in Table III.

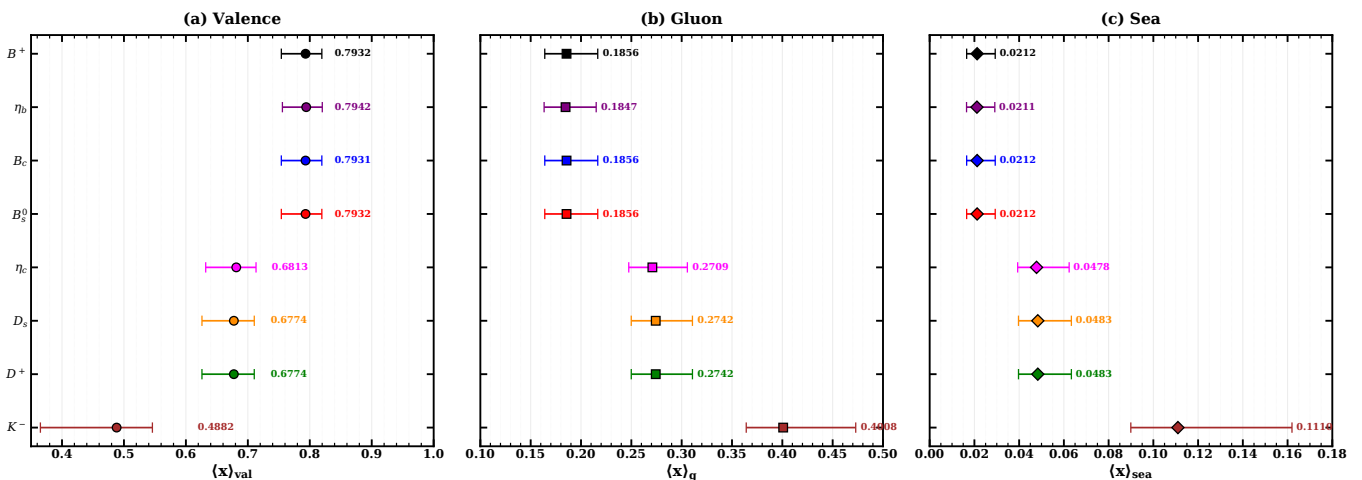
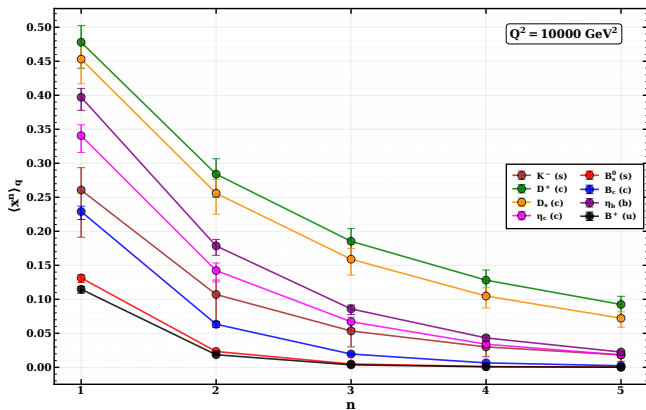


FIG. 16: (Color online) The average momentum fractions carried by the total valence quark-antiquark $\langle x \rangle_{val}$, gluon $\langle x \rangle_g$, and sea-quarks $\langle x \rangle_{sea}$ of different mesons at $Q^2 = 10000 \text{ GeV}^2$. The error band of the momentum fractions is due to the range of the initial scales, which we have considered in this work.

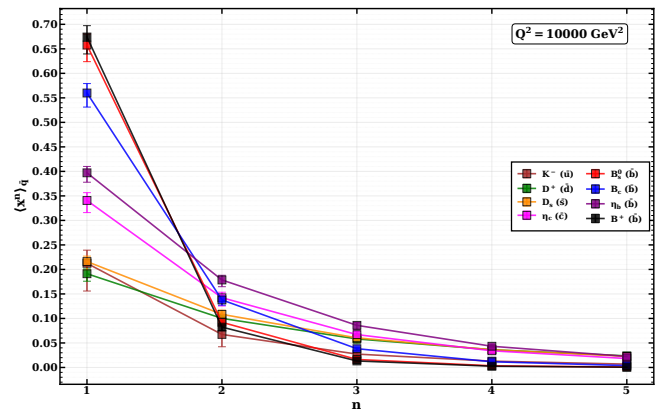
content of the quark-antiquark pair. Therefore, we plot the total heavy quark distribution for charm and bottom in Figs. 10(a) and 11(a), respectively. The inclusion of sea charm quarks enhances the distributions in the low- x region for both charmonium and bottomonium states. In particular, around $x \sim 10^{-5}$, the distributions exhibit a peak of approximately ~ 0.1 . In Figs. 11 - 14, we have plotted the bottom quark content B-mesons (B^+ , B_s^0 and B_c) and bottomonia (η_b) constituent PDFs by taking the initial scale range $Q_0 \in [5.1 - 10.2] \text{ GeV}$ to a higher scale of $Q^2 = 1000$ and 10000 GeV^2 . The constituent PDFs are found to have more concentric (having very little error band width) in the low x region compared to other mesons. This effect is mainly due to the presence of the heavy bottom quark in the mesonic system. The difference between the peak of the valence quark and antiquark PDFs is found to be directly proportional to the mass difference between them. The valence distributions of quarks and antiquarks are found to have maxima in the

low- x region. A similar kind of observation has also been demonstrated in BLFQ for the B_c -meson PDFs [65]. In Figs. 12 (b) and 13 (b), the bottom antiquark is found to carry almost all the momentum fraction compared to the other constituents, indicating the large dominance of the heavy constituent over the lighter mass constituent in the heavy meson case. This can also be observed in the higher Mellin moments case in Figs. 12 (c) and 13 (c). However, for the case of B_c -meson, the dominance of the bottom antiquark is found to be less due to the presence of the charm quark in it, as shown in Fig. 14.

For an overall comparison, we have plotted the valence quark PDF of each meson along with the gluon and sea-quark distributions in Fig. 15 at an energy scale of $Q^2 = 10^4 \text{ GeV}^2$. For the quarkonia case, we have plotted the total quark distributions of the charm and bottom quarks. The heavier quarks are found to have peak distributions in the high x region, while the lighter quarks have distributions in the low x region. This kind of behavior



(a) The Mellin moments of the valence quark of different mesons at $Q^2 = 10000 \text{ GeV}^2$ up to $n = 5$.



(b) The Mellin moments of the valence antiquark of different mesons at $Q^2 = 10000 \text{ GeV}^2$ up to $n = 5$.

FIG. 17: (Color online) The Mellin moments $\langle x^n \rangle$ for the valence quark and valence antiquark distributions of various mesons, evolved to $Q^2 = 10000 \text{ GeV}^2$. The error bands correspond to the scale uncertainty from varying the initial scale Q_0 within its allowed range.

TABLE V: Valence quark momentum asymmetry $\langle x \rangle_q - \langle x \rangle_{\bar{q}}$ at $Q^2 = 10^4 \text{ GeV}^2$ for different meson.

Meson	$\langle x \rangle_{\text{quark}}$	$\langle x \rangle_{\text{antiquark}}$	$\langle x \rangle_q - \langle x \rangle_{\bar{q}}$
K^-	$0.276^{+0.029}_{-0.061}$	$0.228^{+0.024}_{-0.048}$	$0.048^{+0.006}_{-0.012}$
D^+	$0.484^{+0.023}_{-0.036}$	$0.197^{+0.009}_{-0.013}$	$0.287^{+0.014}_{-0.023}$
D_s	$0.459^{+0.022}_{-0.034}$	$0.222^{+0.010}_{-0.015}$	$0.237^{+0.012}_{-0.019}$
η_c	$0.340^{+0.016}_{-0.025}$	$0.341^{+0.016}_{-0.025}$	0.0
B_s^0	$0.134^{+0.004}_{-0.006}$	$0.660^{+0.022}_{-0.033}$	$-0.526^{+0.027}_{-0.018}$
B_c	$0.232^{+0.007}_{-0.010}$	$0.562^{+0.019}_{-0.028}$	$-0.331^{+0.017}_{-0.012}$
η_b	$0.397^{+0.013}_{-0.019}$	$0.397^{+0.013}_{-0.019}$	0.0
B^+	$0.117^{+0.003}_{-0.005}$	$0.678^{+0.023}_{-0.034}$	$-0.559^{+0.029}_{-0.019}$

is also observed at the initial model scale. The gluon and sea-quark distributions of the kaon are found to have higher distributions compared to those of the other mesons. The gluon distributions of all the mesons are found to vanish after $x \geq 0.6$. Similar observations are also seen for the sea-quark distributions of all the mesons. The gluon and sea-quark distributions of quarkonia are found to have a lower distribution compared to others in the low x region. At this scale, we have also calculated the average momentum fraction carried by the valence, gluon and sea-quark PDFs of different mesons in Fig. 16. The momentum fraction carried by the total valence quark and antiquark of the heavy mesons is found to be higher compared to the light mesons. The valence quark and antiquark PDFs of bottomonia and B-mesons are found to carry almost 75% – 83% of the total longitudinal momentum of the mesons, which one can expect from heavy quark systems. At the same time, the valence constituent of the kaon is found to carry 0.35% – 0.55% of the total longitudinal momentum. The sea-quark PDFs are also found to carry less than 10% of the longitudinal momentum in all the heavy mesons except the kaon. So, this much deviation in the longitudinal momentum distribu-

tions between the heavy and light meson cases is totally model-dependent. In Fig. 17, we have plotted the Mellin moments for individual quark and antiquark PDFs of different mesons at the energy scale of 10000 GeV^2 . The first Mellin moment of the quark and antiquark PDFs of different mesons are found to obey the same order as the initial scale as described in Eq. (23). However, the higher order Mellin moments are found to violate that equation. The difference in the momentum fraction carried by the quark and antiquark PDFs $\langle x \rangle_q - \langle x \rangle_{\bar{q}}$ of different mesonic systems at $Q^2 = 1000 \text{ GeV}^2$ and with energy scale range $10^0 \leq Q^2 \leq 10^4$ has also been predicted in Figs. 18 and 19, respectively. This difference in momentum fraction is found to be mass-dependent, as in the initial scale. This difference value has also been presented in the Table. V along with the individual quark and antiquark momentum fraction. This difference in momentum fraction is found to be higher for the B^+ -meson case, where the mass difference between the up and bottom quarks is relatively high compared to others. This difference is found to decrease more for the heavy B-mesons than for other mesons, as shown in Fig. 19. For the kaon, the quark-antiquark momentum asymmetry shows very weak scale

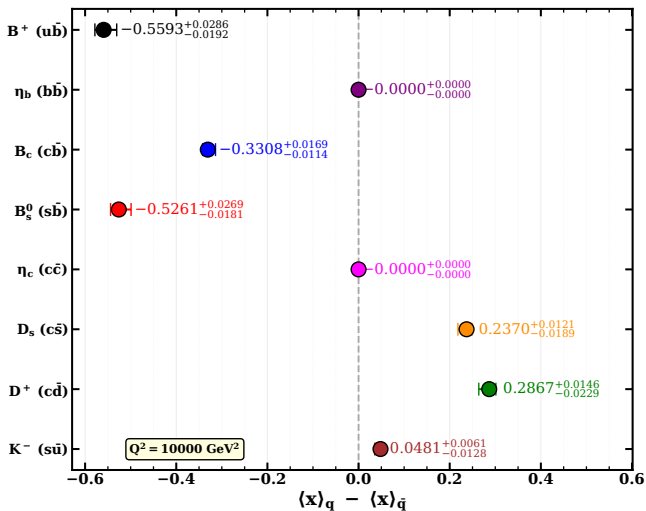


FIG. 18: (Color online) The difference in the valence quark and antiquark momentum fractions $\langle x \rangle_q - \langle x \rangle_{\bar{q}}$ of different mesons at $Q^2 = 10000 \text{ GeV}^2$.

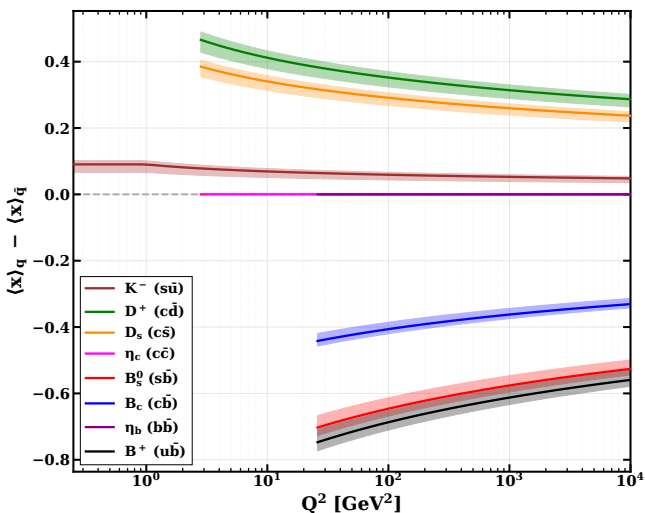


FIG. 19: (Color online) The difference in the valence quark and antiquark momentum fractions $\langle x \rangle_q - \langle x \rangle_{\bar{q}}$ of different mesons with respect to Q^2 (GeV^2).

dependence and remains nearly constant under DGLAP evolution. The magnitude of the quark-antiquark momentum asymmetry $|\langle x \rangle_q - \langle x \rangle_{\bar{q}}|$ across different mesons follows the hierarchy

$$B^+ > B_s^0 > B_c > D^+ > D_s > K^-. \quad (33)$$

We have also demonstrated the behavior of bottom and charm PDFs in Figs. 21 and 20, respectively. The bottom antiquark PDFs plotted in Fig. 21 are found to have different distributions for different mesons. The bottom antiquark PDFs are peaked at large- x due to the presence of a heavy quark, while the peak shifts toward lower- x as

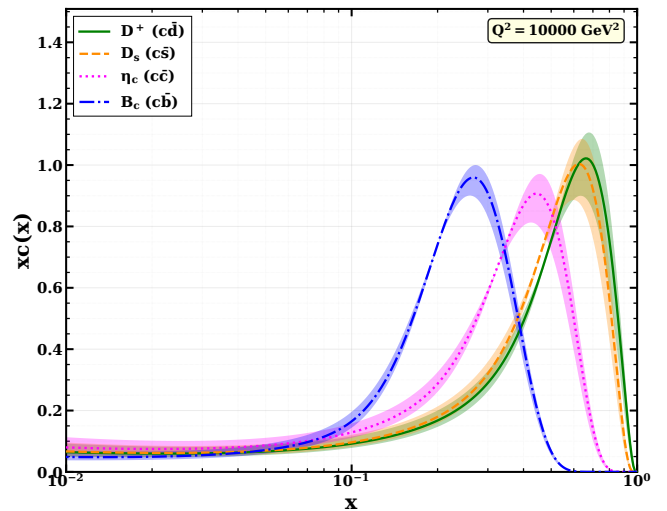


FIG. 20: (Color online) Behavior of the charm parton distribution $x c(x)$ as a function of x at $Q^2 = 10^4 \text{ GeV}^2$ for the $D^+ (c\bar{d})$, $D_s^+ (c\bar{s})$, $\eta_c (c\bar{c})$, and $B_c^+ (c\bar{b})$ mesons.

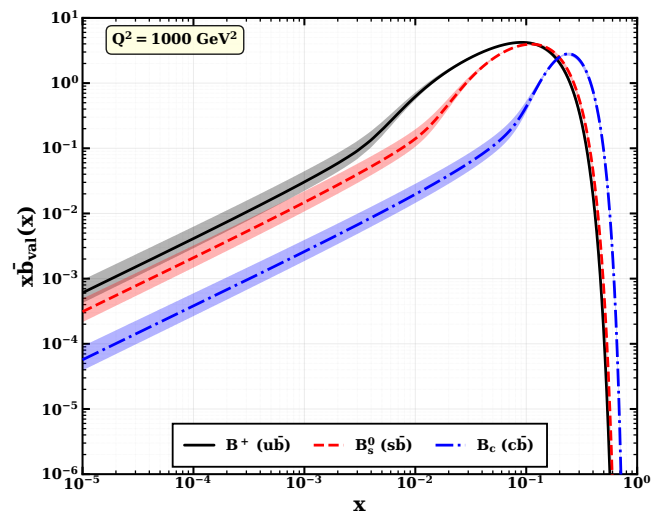


FIG. 21: (Color online) Behavior of the bottom parton distribution $x b(x)$ as a function of x at $Q^2 = 10^4 \text{ GeV}^2$ for the B-mesons.

the mass of the partner quark decreases. Similar observations are also found for the charm quark PDFs in Fig. 20. In Fig. 22, we have plotted the top sea-quark distributions from different mesonic systems by taking the energy scale $Q^2(10^5) > m_t^2$ (GeV^2). At such scales, the top sea-quark distributions are generated perturbatively via gluon splitting $g \rightarrow t\bar{t}$. The observed enhancement of the top sea-quark distribution for the kaon reflects its comparatively larger gluon density after DGLAP evolution, originating from its distinct initial parton distributions as shown in Fig. 22.

Overall, the PDFs of various mesons exhibit distinct structural features that reflect differences in their flavor

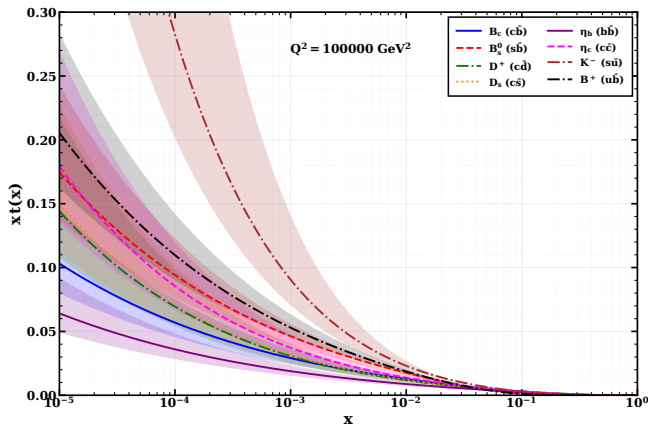


FIG. 22: (Color online) The distribution of top sea-quark PDFs for different mesons at the scale of 10^5 GeV^2 .

compositions and internal quark–gluon dynamics. One possible concern may arise from the choice of different initial scales, Q_0 , used for the QCD evolution of different mesons. To examine the sensitivity of our results to this choice, we also performed the evolution using a common initial scale for all mesons. We observed that both the overall numerical behavior and the qualitative features of the PDFs remain largely unchanged. This indicates that the observed differences among the meson PDFs are primarily governed by their underlying non-perturbative structures rather than by the specific choice of the initial evolution scale.

IV. CONCLUSION

In this work, we have investigated the parton distribution functions (PDFs) of pseudoscalar mesons both at the initial scale and after QCD evolution to higher scales. The quark and antiquark PDFs at the initial scale have been calculated within the light-cone quark model (LCQM) using the Brodsky–Huang–Lepage momentum-space wave functions. By solving the quark–quark correlation functions, we obtained explicit expressions for the quark and antiquark PDFs. The QCD evolution of the PDFs from the initial to higher scales has been performed using the next-to-leading-order (NLO) DGLAP evolution

equations through the HOPPET toolkit. The calculated quark and antiquark PDFs are found to satisfy the required sum rules. For the evolution, we considered an initial-scale band whose lower limit is taken to be equal to the heavy constituent quark mass.

The PDFs corresponding to heavier constituent quarks are found to peak in the large- x region, whereas the PDFs associated with lighter constituents exhibit maximum distributions in the low- x region. In the case of symmetric quark–antiquark systems, the distributions are found to be symmetric around $x = 0.5$. The heavy mesons are observed to possess smaller gluon and sea-quark distributions compared to the lighter mesons. The valence PDFs dominate in the region $x \gtrsim 0.2$, while the gluon and sea-quark distributions become dominant in the low- x region. For asymmetric quark–antiquark meson systems, the heavier constituent is found to dominate over the lighter one and carries a larger fraction of the longitudinal momentum of the meson. Moreover, the same quark flavor exhibits different distributions in different mesonic systems.

For the kaon case, we have also presented predictions for the NLO structure functions relevant to the upcoming Electron–Ion colliders (EICs) through tagged deep-inelastic scattering processes, along with the differential Drell–Yan cross sections for different nuclear targets relevant to the future COMPASS++/AMBER experiments. The calculated Mellin moments are found to be in good agreement with other theoretical studies and lattice QCD simulations. However, in the heavy-meson sector, it remains challenging to constrain the PDFs directly from experimental data. Consequently, further progress in this direction will strongly rely on complementary inputs from theoretical models and lattice QCD simulations.

Acknowledgment

The author sincerely acknowledges valuable discussions and insightful suggestions from Craig D. Roberts, Wen-Chen Chang, Chia-Yu Hsieh, Marco Meyer-Conde, Narinder Kumar, Ashutosh Dwivedi, and Shubham Sharma. The author especially thanks Ashutosh Dwivedi and Shubham Sharma for carefully reading the manuscript and providing useful comments and suggestions.

-
- [1] S. J. Brodsky, H.-C. Pauli, and S. S. Pinsky, Phys. Rept. **301**, 299 (1998), hep-ph/9705477.
 [2] H. Mineo, W. Bentz, N. Ishii, A. W. Thomas, and K. Yazaki, Nucl. Phys. A **735**, 482 (2004), nucl-th/0312097.
 [3] Y. Nambu and G. Jona-Lasinio, Phys. Rev. **122**, 345 (1961).
 [4] S. P. Klevansky, Rev. Mod. Phys. **64**, 649 (1992).

- [5] F. Schlumpf, Phys. Rev. D **50**, 6895 (1994), hep-ph/9406267.
 [6] S. J. Brodsky and G. F. de Teramond, Phys. Rev. Lett. **96**, 201601 (2006), hep-ph/0602252.
 [7] C. D. Roberts and S. M. Schmidt, Prog. Part. Nucl. Phys. **45**, S1 (2000).
 [8] X. Ji, G. A. Miller, and C. Yang (2026), 2605.00339.
 [9] S. Meissner, A. Metz, and M. Schlegel, JHEP **08**, 056

- (2009), 0906.5323.
- [10] K. Goeke, A. Metz, and M. Schlegel, *Phys. Lett. B* **618**, 90 (2005), hep-ph/0504130.
- [11] S. Puhan, S. Sharma, N. Kumar, and H. Dahiya (2025), 2504.14982.
- [12] M. Diehl, *Phys. Rept.* **388**, 41 (2003), hep-ph/0307382.
- [13] J. M. M. Chavez, V. Bertone, F. De Soto Borrero, M. Defurne, C. Mezrag, H. Moutarde, J. Rodríguez-Quintero, and J. Segovia, *Phys. Rev. D* **105**, 094012 (2022), 2110.06052.
- [14] J.-L. Zhang and J.-L. Ping, *Eur. Phys. J. C* **81**, 814 (2021).
- [15] W. Broniowski, V. Shastry, and E. Ruiz Arriola, *Phys. Lett. B* **840**, 137872 (2023), 2211.11067.
- [16] M. Guidal, M. V. Polyakov, A. V. Radyushkin, and M. Vanderhaeghen, *Phys. Rev. D* **72**, 054013 (2005), hep-ph/0410251.
- [17] S. Puhan, S. Sharma, N. Kumar, and H. Dahiya (2026), 2604.11116.
- [18] M. Diehl, *Eur. Phys. J. A* **52**, 149 (2016), 1512.01328.
- [19] R. Angeles-Martinez et al., *Acta Phys. Polon. B* **46**, 2501 (2015), 1507.05267.
- [20] B. Pasquini, S. Cazzaniga, and S. Boffi, *Phys. Rev. D* **78**, 034025 (2008), 0806.2298.
- [21] S. Puhan, S. Sharma, N. Kaur, N. Kumar, and H. Dahiya, *JHEP* **02**, 075 (2024), 2310.03464.
- [22] S. Puhan and H. Dahiya, *Phys. Rev. D* **109**, 034005 (2024), 2310.03465.
- [23] S. Puhan, S. Sharma, N. Kumar, and H. Dahiya, *Phys. Rev. D* **113**, 036030 (2026), 2511.10981.
- [24] J. C. Collins and D. E. Soper, *Nucl. Phys. B* **194**, 445 (1982).
- [25] A. D. Martin, R. G. Roberts, W. J. Stirling, and R. S. Thorne, *Eur. Phys. J. C* **4**, 463 (1998), hep-ph/9803445.
- [26] M. Gluck, E. Reya, and A. Vogt, *Z. Phys. C* **67**, 433 (1995).
- [27] S. Puhan and H. Dahiya, *Phys. Rev. D* **111**, 114039 (2025), 2505.02507.
- [28] J. Arrington, C. D. Roberts, and J. M. Zanotti, *J. Phys. G* **34**, S23 (2007), nucl-th/0611050.
- [29] P. C. e. a. Barry, *Phys. Rev. Lett.* **121**, 152001 (2018).
- [30] E. D. Bloom et al., *Phys. Rev. Lett.* **23**, 930 (1969).
- [31] G. Altarelli and G. Parisi, *Nucl. Phys. B* **126**, 298 (1977).
- [32] F. D. Aaron et al. (H1), *Eur. Phys. J. C* **68**, 381 (2010), 1001.0532.
- [33] S. Chekanov et al. (ZEUS), *Nucl. Phys. B* **637**, 3 (2002), hep-ex/0205076.
- [34] M. Bonesini et al. (WA70), *Z. Phys. C* **37**, 535 (1988).
- [35] W.-C. Chang, J.-C. Peng, S. Platchkov, and T. Sawada, *Phys. Rev. D* **107**, 056008 (2023), 2209.04072.
- [36] S. D. Drell and T.-M. Yan, *Phys. Rev. Lett.* **25**, 316 (1970), [Erratum: *Phys.Rev.Lett.* 25, 902 (1970)].
- [37] C. Lorcé, A. Metz, B. Pasquini, and P. Schweitzer (2025), 2507.12664.
- [38] G. Aad et al. (ATLAS), *JHEP* **07**, 223 (2021), 2101.05095.
- [39] H. G. P, S. Puhan, A. K. P, R. Pandey, H. Dahiya, A. Kumar, and S. Dutt (2026), 2604.05762.
- [40] J. Lan, C. Mondal, S. Jia, X. Zhao, and J. P. Vary, *Phys. Rev. D* **101**, 034024 (2020), 1907.01509.
- [41] T. Gutsche, V. E. Lyubovitskij, I. Schmidt, and A. Vega, *J. Phys. G* **42**, 095005 (2015), 1410.6424.
- [42] C. Shi, L. Lu, and W. Jia (2026), 2602.24187.
- [43] J. S. Conway et al. (E615), *Phys. Rev. D* **39**, 92 (1989).
- [44] C. Bourrely, W.-C. Chang, and J.-C. Peng, *Phys. Rev. D* **105**, 076018 (2022), 2202.12547.
- [45] P. C. Barry, C.-R. Ji, N. Sato, and W. Melnitchouk (Jefferson Lab Angular Momentum (JAM)), *Phys. Rev. Lett.* **127**, 232001 (2021), 2108.05822.
- [46] W.-C. Chang, J.-C. Peng, S. Platchkov, and T. Sawada, *Phys. Rev. D* **102**, 054024 (2020), 2006.06947.
- [47] I. Novikov et al., *Phys. Rev. D* **102**, 014040 (2020), 2002.02902.
- [48] M. Gluck, E. Reya, and I. Schienbein, *Eur. Phys. J. C* **10**, 313 (1999), hep-ph/9903288.
- [49] J. Miller, J. Torsiello, I. Anderson, K. Cichy, M. Constantinou, J. Delmar, and S. Lampreich (2025), 2512.06121.
- [50] C. Alexandrou et al. (Extended Twisted Mass), *Phys. Rev. Lett.* **134**, 131902 (2025), 2405.08529.
- [51] Y. Choi, A. J. Arifi, H.-M. Choi, and C.-R. Ji (2025), 2512.21642.
- [52] G. F. de Teramond and S. J. Brodsky, *Phys. Rev. Lett.* **102**, 081601 (2009), 0809.4899.
- [53] M. Ding, K. Raya, D. Binosi, L. Chang, C. D. Roberts, and S. M. Schmidt, *Phys. Rev. D* **101**, 054014 (2020), 1905.02508.
- [54] S.-i. Nam, *Phys. Rev. D* **86**, 074005 (2012), 1205.4156.
- [55] P. C. Barry, C.-R. Ji, W. Melnitchouk, N. Sato, and F. Steffens (JAM) (2025), 2510.11979.
- [56] W.-C. Chang, J.-C. Peng, S. Platchkov, and T. Sawada, *Phys. Lett. B* **855**, 138820 (2024), 2402.02860.
- [57] C. Bourrely, F. Buccella, W.-C. Chang, and J.-C. Peng, *Phys. Lett. B* **848**, 138395 (2024), 2305.18117.
- [58] J. Badiar et al. (Saclay-CERN-College de France-Ecole Poly-Orsay), *Phys. Lett. B* **93**, 354 (1980).
- [59] M. J. Corden et al., *Phys. Lett. B* **96**, 411 (1980).
- [60] B. Adams et al. (2018), 1808.00848.
- [61] Z. Lu, Z. Yu, T. Lin, Y.-T. Liang, R. Wang, W. Chang, and W. Xiong (2025), 2512.01720.
- [62] A. C. Aguilar et al., *Eur. Phys. J. A* **55**, 190 (2019), 1907.08218.
- [63] Q. Wu, Z.-F. Cui, and J. Segovia, *Phys. Rev. D* **111**, 116023 (2025), 2503.07055.
- [64] L. Albino, I. M. Higuera-Angulo, K. Raya, and A. Bashir, *Phys. Rev. D* **106**, 034003 (2022), 2207.06550.
- [65] J. Lan, C. Mondal, M. Li, Y. Li, S. Tang, X. Zhao, and J. P. Vary, *Phys. Rev. D* **102**, 014020 (2020), 1911.11676.
- [66] S. Tang, Y. Li, P. Maris, and J. P. Vary, *Eur. Phys. J. C* **80**, 522 (2020), 1912.02088.
- [67] C. Shi, P. Liu, Y.-L. Du, and W. Jia, *Phys. Rev. D* **110**, 094010 (2024), 2409.05098.
- [68] S. Puhan and H. Dahiya, *PoS HQL2023*, 089 (2024), 2408.07717.
- [69] C. Shi, J. Li, M. Li, X. Chen, and W. Jia, *Phys. Rev. D* **106**, 014026 (2022), 2205.02757.
- [70] A. Karlberg, P. Nason, G. Salam, G. Zanderighi, and F. Dreyer, *Eur. Phys. J. C* **86**, 157 (2026), 2510.09310.
- [71] A. Buckley, J. Ferrando, S. Lloyd, K. Nordström, B. Page, M. Rüfenacht, M. Schönherr, and G. Watt, *Eur. Phys. J. C* **75**, 132 (2015), 1412.7420.
- [72] M. B. Hecht, C. D. Roberts, and S. M. Schmidt, *Phys. Rev. C* **63**, 025213 (2001), nucl-th/0008049.
- [73] G. P. Lepage and S. J. Brodsky, *Phys. Rev. D* **22**, 2157 (1980).

- [74] X.-d. Ji, J.-P. Ma, and F. Yuan, *Eur. Phys. J. C* **33**, 75 (2004), hep-ph/0304107.
- [75] S. J. Brodsky, M. Diehl, and D. S. Hwang, *Nucl. Phys. B* **596**, 99 (2001), hep-ph/0009254.
- [76] S. J. Brodsky, H.-C. Pauli, and S. S. Pinsky, *Phys. Rept.* **301**, 299 (1998), hep-ph/9705477.
- [77] B. Pasquini, S. Rodini, and S. Venturini (MAP (Multi-dimensional Analyses of Partonic distributions)), *Phys. Rev. D* **107**, 114023 (2023), 2303.01789.
- [78] X. Luan and Z. Lu, *Phys. Rev. D* **110**, 074022 (2024), 2406.19376.
- [79] W. Qian and B.-Q. Ma, *Phys. Rev. D* **78**, 074002 (2008), 0809.4411.
- [80] Tanisha, S. Puhan, A. Yadav, and H. Dahiya, *Phys. Rev. D* **112**, 054035 (2025), 2505.09213.
- [81] S. Puhan, N. Kaur, and H. Dahiya, *Phys. Rev. D* **111**, 014008 (2025), 2410.07596.
- [82] R. Acharyya, S. Puhan, and H. Dahiya, *Phys. Rev. D* **110**, 034020 (2024), 2405.00446.
- [83] G. P. Lepage and S. J. Brodsky, *Phys. Rev. D* **22**, 2157 (1980).
- [84] S. J. Brodsky, Y. Frishman, G. P. Lepage, and C. T. Sachrajda, *Phys. Lett. B* **91**, 239 (1980).
- [85] B.-W. Xiao, X. Qian, and B.-Q. Ma, *Eur. Phys. J. A* **15**, 523 (2002), hep-ph/0209138.
- [86] S. Puhan, N. Kaur, A. Kumar, S. Dutt, and H. Dahiya, *Nucl. Phys. B* **1017**, 116940 (2025), 2501.16706.
- [87] A. J. Arifi, H.-M. Choi, C.-R. Ji, and Y. Oh, *Phys. Rev. D* **106**, 014009 (2022), 2205.04075.
- [88] H. M. Choi and C.-R. Ji, *Nucl. Phys. A* **618**, 291 (1997).
- [89] A. Dwivedi, S. Puhan, S. Ghosh, and H. Dahiya (2025), 2512.24921.
- [90] A. Harindranath, in *International School on Light-Front Quantization and Non-Perturbative QCD (To be followed by the Workshop 3-14 Jun 1996)* (1996), hep-ph/9612244.
- [91] C. Chen, L. Chang, C. D. Roberts, S. Wan, and H.-S. Zong, *Phys. Rev. D* **93**, 074021 (2016), 1602.01502.
- [92] A. Watanabe, T. Sawada, and C. W. Kao, *Nucl. Part. Phys. Proc.* **300-302**, 121 (2018), 1810.04032.
- [93] C. Alexandrou, S. Bacchio, I. Cloët, M. Constantinou, K. Hadjiyiannakou, G. Koutsou, and C. Lauer (ETM), *Phys. Rev. D* **104**, 054504 (2021), 2104.02247.
- [94] K. Kovarik et al., *Phys. Rev. D* **93**, 085037 (2016), 1509.00792.
- [95] T. Maji and D. Chakrabarti, *Phys. Rev. D* **94**, 094020 (2016), 1608.07776.
- [96] A. Bacchetta, F. G. Celiberto, M. Radici, and P. Taelis, *Eur. Phys. J. C* **80**, 733 (2020), 2005.02288.
- [97] C. Shi, M. Li, X. Chen, and W. Jia, *Phys. Rev. D* **104**, 094016 (2021), 2108.10625.
- [98] R. Acharyya, S. Puhan, H. Dahiya, and N. Kumar, *Chin. Phys. C* **49**, 023104 (2025), 2408.07715.
- [99] Y. Li, P. Maris, X. Zhao, and J. P. Vary, *Phys. Lett. B* **758**, 118 (2016), 1509.07212.
- [100] Y. Li, P. Maris, and J. P. Vary, *Phys. Rev. D* **96**, 016022 (2017), 1704.06968.
- [101] S. Tang, Y. Li, P. Maris, and J. P. Vary, *Phys. Rev. D* **98**, 114038 (2018), 1810.05971.
- [102] B. Almeida-Zamora, L. Albino, A. Bashir, J. J. Cobos-Martínez, and J. Segovia (2026), 2602.10775.
- [103] G. P. Salam and J. Rojo, *Comput. Phys. Commun.* **180**, 120 (2009), 0804.3755.
- [104] V. N. Gribov and L. N. Lipatov, *Sov. J. Nucl. Phys.* **15**, 438 (1972).
- [105] L. N. Lipatov, *Sov. J. Nucl. Phys.* **20**, 94 (1975).
- [106] Y. L. Dokshitzer, *Sov. Phys. JETP* **46**, 641 (1977).
- [107] T. Horn and K. e. a. Park, *Tech. Rep. C12-15-006A*, Jefferson Lab (2015), accessed: 2021-09-16, URL https://www.jlab.org/exp_prog/proposals/17/C12-15-006A.pdf.
- [108] C. Anastasiou, L. J. Dixon, K. Melnikov, and F. Petriello, *Phys. Rev. Lett.* **91**, 182002 (2003), hep-ph/0306192.
- [109] J. Lan, J. Chen, Z. Zhu, C. Mondal, X. Zhao, and J. P. Vary (BLFQ), *Phys. Lett. B* **868**, 139654 (2025), 2501.03476.
- [110] X. Chen, *PoS DIS2018*, 170 (2018), 1809.00448.
- [111] E. C. Aschenauer et al. (2014), 1409.1633.
- [112] J. L. Abelleira Fernandez et al. (LHeC Study Group), *J. Phys. G* **39**, 075001 (2012), 1206.2913.